

**DUAL WAVELENGTH POLARIMETRY FOR GLUCOSE SENSING IN THE
ANTERIOR CHAMBER OF THE EYE**

A Dissertation

by

BILAL HAMEED MALIK

Submitted to the Office of Graduate Studies of
Texas A&M University
in partial fulfillment of the requirements for the degree of

DOCTOR OF PHILOSOPHY

December 2011

Major Subject: Biomedical Engineering

Dual Wavelength Polarimetry for Glucose Sensing in the Anterior Chamber of the Eye

Copyright 2011 Bilal Hameed Malik

**DUAL WAVELENGTH POLARIMETRY FOR GLUCOSE SENSING IN THE
ANTERIOR CHAMBER OF THE EYE**

A Dissertation

by

BILAL HAMEED MALIK

Submitted to the Office of Graduate Studies of
Texas A&M University
in partial fulfillment of the requirements for the degree of

DOCTOR OF PHILOSOPHY

Approved by:

Chair of Committee,	Gerard L. Coté
Committee Members,	Kenith E. Meissner
	Brian E. Applegate
	Chin B. Su
Head of Department,	Gerard L. Coté

December 2011

Major Subject: Biomedical Engineering

ABSTRACT

Dual Wavelength Polarimetry for Glucose Sensing in the Anterior Chamber of the Eye.

(December 2011)

Bilal Hameed Malik, B.S., GIK Institute; M.S., Texas A&M University

Chair of Advisory Committee: Dr. Gerard L. Coté

Clinical guidelines dictate that frequent blood glucose monitoring in diabetic patients is critical towards proper management of the disease. Although several different types of glucose monitors are now commercially available, most of these devices are invasive, thereby adversely affecting patient compliance. To this end, optical polarimetric glucose sensing through the eye is proposed as a potential noninvasive means to aid in the control of diabetes. Arguably, the most critical and limiting factor towards successful application of such a technique is the time varying corneal birefringence due to eye motion artifact.

In the first part of this research, we describe a birefringent ocular model along with a geometric ray tracing scheme to serve as a tool toward better understanding of the cornea's birefringence properties. The simulations show that index-unmatched coupling of light is spatially limited to a smaller range when compared to an index-matched situation. Polarimetric measurements on rabbits' eyes indicate relative agreement between the modeled and experimental values of corneal birefringence. In addition, the observed rotation in the plane of polarized light for multiple wavelengths demonstrates

the potential for using a dual-wavelength polarimetric approach to overcome the noise due to time-varying corneal birefringence. These results ultimately aid in the development of an appropriate eye coupling mechanism for *in vivo* polarimetric glucose measurements.

The latter part of the dissertation focuses on design and development of a dual wavelength optical polarimeter. The described system utilizes real-time closed-loop feedback based on proportional-integral-derivative (PID) control, which effectively reduces the time taken by the system to stabilize while minimizing the effect of motion artifact, which appears as a common noise source for both wavelengths. Glucose measurements performed in both *in vitro* and *ex vivo* conditions demonstrate the sensitivity of the current system. Finally, *in vivo* results in rabbits indicate that dual-wavelength polarimetry has the potential to noninvasively probe glucose through the anterior chamber of the eye.

DEDICATION

To my wife, Nadia.

ACKNOWLEDGEMENTS

First and foremost, I would like to thank my committee chair, Dr. Gerard Coté, for his guidance and support through the course of this research. Throughout the four years, he helped to keep my thinking sharp and my standards of evidence high, and I could not have asked for a better mentor and advisor.

I would also like to thank Dr. Meissner, Dr. Applegate, and Dr. Su for the helpful discussions, and for volunteering their time to serve as members of my graduate committee. My appreciation is also extended to Dr. Gresham for his training and his active cooperation in this research. None of these professors needed to spend so much of their busy lives guiding me as they did, and I will be forever indebted to them for what they taught me about the essence and development of scholarship.

Thanks also go to my friends, including but not limited to, Tony Akl, Melodie Benford, Brian Cummins, Casey Pirstill, and Dustin Ritter, for making my time at Texas A&M University a great experience. They have been extraordinarily helpful and selfless colleagues.

Finally, my deepest gratitude is to my family – my wife, Nadia, and our daughter, Aimen. In the last four years, they had to endure the most in terms of my time away from home, and I am forever grateful for their love and support.

TABLE OF CONTENTS

	Page
ABSTRACT	iii
DEDICATION	v
ACKNOWLEDGEMENTS	vi
TABLE OF CONTENTS	vii
LIST OF FIGURES.....	ix
CHAPTER I INTRODUCTION	1
Diabetes Mellitus: Disease and Therapy.....	1
Noninvasive Glucose Sensing.....	5
Polarimetric Glucose Sensing.....	7
CHAPTER II THEORY.....	11
Fundamentals of Light Polarization.....	11
Optical Activity and Polarimetry.....	11
Anterior Chamber of the Eye.....	16
Corneal Birefringence.....	18
CHAPTER III MODELING OF CORNEAL BIREFRINGENCE.....	21
Introduction.....	21
Materials and Methods.....	24
Index-matched Coupling of Light.....	27
Index-unmatched Coupling of Light.....	29
Experimental Setup to Measure the Effect of Corneal Birefringence.....	31
Results and Discussion.....	33
Index-matched Coupling of Light.....	33
Index-unmatched Coupling of Light.....	41
Experimental Measurement of the Effect of Corneal Birefringence.....	46
CHAPTER IV POLARIMETRIC GLUCOSE SENSING.....	51
Introduction.....	51
Materials and Methods.....	52

	Page
Dual Wavelength Polarimeter	52
Control System	56
Faraday Rotators.....	57
Eye Coupling Mechanism	57
Plastic Eye Model.....	59
Ex Vivo Mounted Corneas	61
In Vivo Animal Studies	62
Results and Discussion.....	65
In Vitro Experiments using Glucose Samples in a Cuvette	65
In Vitro Experiments using Plastic Ocular Phantom.....	73
Ex Vivo Experiments using Isolated Corneas	76
In Vivo Experiments in Rabbits	80
CHAPTER V CONCLUSIONS AND FUTURE WORK	88
REFERENCES	91
APPENDIX A	103
VITA	104

LIST OF FIGURES

	Page
Figure 1. Picture of FreeStyle Navigator continuous glucose monitoring system.....	4
Figure 2. Schematic representation of glucose forms in solution.	13
Figure 3. A basic polarimeter comprised of two crossed polarizers with the sample placed in between them.	15
Figure 4. Aqueous humor flows continuously in and out of the anterior chamber and nourishes nearby tissues.	17
Figure 5. Cross section of the human cornea.	19
Figure 6. Representative dimensions of the human eye model.	25
Figure 7. Local Cartesian coordinate system at an arbitrary point P on the posterior corneal surface.	27
Figure 8. Optical path through the anterior chamber of the eye.	28
Figure 9. Optical path through the anterior chamber of the eye for unmatched refractive indices.....	30
Figure 10. Optical configuration for experimental measurement of corneal birefringence.	32
Figure 11. (a) Angle of major axis of the output beam polarization ellipse as a function of distance from the apex of the cornea.	34
Figure 12. Variation in state of polarization as a function of distance from the corneal apex.....	35
Figure 13. (a) Change in optical path length through the aqueous humor as a function of distance from the apex of the cornea, and (b) corresponding net rotation in angle of polarization vector as a function of distance from the apex of the cornea.....	37
Figure 14. Net rotation in the angle of polarization vector as a function of glucose concentration.....	38
Figure 15. Angle of major axes for wavelengths of 635 (solid line) and 532 nm (dashed line) as a function of distance from the apex of the cornea.	40

	Page
Figure 16. Angle of major axis of polarization ellipse as a function of angle of incidence for beam position at (a) 2.5 mm, (b) 2.0 mm, and (c) 1.6 mm below the corneal apex.	42
Figure 17. Optical path through the anterior chamber of the eye for beam position and angle of incidence at (a) 1.6 mm and 16°, (b) 2.0 mm and 23°, and (c) 2.5 mm and 28°, respectively.....	44
Figure 18. Inter-eye variation of measured angle of major axis of polarization ellipse as a function of wavelength.	47
Figure 19. Intra-eye variation of measured angle of major axis of polarization ellipse as a function of wavelength and angle of incidence.	49
Figure 20. Experimental setup of the dual-wavelength optical polarimeter.	54
Figure 21. Photograph (left) and CAD model (right) of the eye coupling device.	58
Figure 22. Photograph of the custom-built ocular model.....	60
Figure 23. Photograph of an isolated cornea clamped on the artificial anterior chamber.....	61
Figure 24. Photograph of the eye coupling device.....	63
Figure 25. Photograph of the eye coupling device placed on the rabbit eye.....	64
Figure 26. Mean estimated glucose concentration as a function of actual glucose concentration for an open-loop single wavelength model using the 635 nm wavelength.	66
Figure 27. Mean estimated glucose concentration as a function of actual glucose concentration for an open-loop single wavelength model using the 830 nm wavelength.	67
Figure 28. Mean predicted glucose concentrations for the real-time open-loop dual wavelength system using a multi-regression model.	68
Figure 29. Mean estimated glucose concentration as a function of actual glucose concentration for a closed-loop single wavelength model using the 635 nm wavelength.....	70

	Page
Figure 30. Mean estimated glucose concentration as a function of actual glucose concentration for a closed-loop single wavelength model using the 830 nm wavelength.	71
Figure 31. Mean predicted glucose concentrations for the real-time closed-loop dual wavelength system using a multi-regression model.	72
Figure 32. Mean estimated glucose concentration as a function of actual glucose concentration for the <i>in vitro</i> single wavelength model using (a) 635-nm, and (b) 532-nm wavelengths.	74
Figure 33. Mean estimated glucose concentration as a function of actual glucose concentration for the <i>in vitro</i> dual wavelength model.	75
Figure 34. Mean estimated glucose concentration as a function of actual glucose concentration for the <i>ex vivo</i> single wavelength model using (a) 635-nm, and (b) 532-nm wavelengths.	77
Figure 35. Mean estimated glucose concentration as a function of actual glucose concentration for the <i>ex vivo</i> dual wavelength model.	78
Figure 36. Blood glucose response in NZW rabbits after administration of anesthesia ..	80
Figure 37. Spectral analysis of the time-based polarimetric feedback signal – Run 1; top: 635-nm feedback, bottom: 532-nm feedback.	82
Figure 38. Spectral analysis of the time-based polarimetric feedback signal – Run 2; top: 635-nm feedback, bottom: 532-nm feedback.	83
Figure 39. Predicted glucose concentration as a function of actual glucose concentration for the single wavelength model using the 635-nm wavelength.	85
Figure 40. Predicted glucose concentration as a function of actual glucose concentration for the single wavelength model using the 532-nm wavelength.	86
Figure 41. Predicted glucose concentration as a function of actual glucose concentration for the dual wavelength model.	87

CHAPTER I

INTRODUCTION

Diabetes Mellitus: Disease and Therapy

Diabetes mellitus is a chronic disease, which is marked by high levels of blood glucose levels resulting from defects in insulin production, insulin action, or both. It currently afflicts over 345 million people worldwide, and over 25 million in the United States [1, 2]. In the U.S. this disorder, along with its associated complications, is ranked as the seventh leading cause of death. As of 2007, the estimated direct and indirect cost of this disease is \$174 billion per year [2]. Self-monitoring of blood glucose is recommended for diabetic patients as the current standard of care and, since the announcement of the Diabetes Control and Complications Trial results, there is now no question that intensive management of blood sugars is an effective means to prevent or at least slow the progression of diabetic complications such as kidney failure, heart disease, gangrene, and blindness [3].

The goal of diabetes therapy is to approximate the blood glucose profile of a normal individual. Without regulation, hypoglycemia, a condition in which the blood glucose level falls well below normal, may cause the patient to slip into a coma and eventual death. Alternatively, a condition known as hyperglycemia can develop in

This dissertation follows the style of Biomedical Optics Express.

which blood glucose levels can rise considerably above normal levels. If left untreated, these abnormally high blood glucose levels may result in long-term complications such as an increased risk of coronary artery disease, hypertension, retinopathy, neuropathy, and nephropathy [3, 4]. Research indicates that some of these long-term complications can be minimized if diabetes is properly treated [4]. Proper treatment includes maintaining blood glucose levels near normal levels. This can only be achieved with frequent blood glucose monitoring so that appropriate actions can be taken, such as insulin injections, proper diet, or exercise.

The current commercially available methods of glucose sensing are usually based on colorimetric or electrochemical schemes, which are invasive, requiring a finger stick to draw blood each time a reading is needed [5]. This approach is both time-consuming, painful, raises concerns about blood borne pathogens, and can be embarrassing. Thus, unfortunately, it is frequently difficult to obtain the appropriate motivation and dedication on the part of the diabetic patients for them to commit to an intensive program of blood sugar monitoring.

Continuous glucose monitoring (CGM) is now available commercially for use as a trending monitor for the management of diabetes. Recent trials using CGM suggest significant improvements in important clinical outcomes such as hemoglobin A1c, time spent in the hypo- and hyperglycemic range, and perceived value to physicians and patients [6-8]. To this end, several different CGM devices are now commercially available [9, 10]. One of the first noninvasive CGM sensors to be approved by Food and Drug Administration (FDA) was the GlucoWatch developed by Cygnus and

subsequently sold to Animas Technologies, which is currently part of Johnson and Johnson. This device utilizes reverse iontophoresis to measure glucose concentration in the subcutaneous fluid [9]. Although termed noninvasive, the iontophoretic current disrupts the skin surface, and can cause skin irritation. It also takes up to 20 minutes to gather enough fluid to make the measurement. These actually turned out to be major drawbacks and the GlucoWatch technology has been withdrawn from commercial distribution [9]. Another noninvasive CGM sensor known as PENDRA was released in European markets to be used in conjunction with finger stick blood glucose monitor [11]. This device employs impedance spectroscopy at the skin surface whereby a small AC current induces impedance changes within the skin and underlying tissues, which are correlated to glucose concentration. Although initial studies and assessments of the device were promising, post-market trials and investigations indicated poor accuracy, which ultimately resulted in withdrawal from commercial distribution [11-13].

Most of the currently available commercial CGM devices are minimally invasive [10]. MiniMed was the first company to obtain FDA approval as a trending monitor for a CGM device and was purchased by Medtronic in 2001[9]. Their current CGM system called Guardian RT is an amperometric device which provides glucose measurements in real-time. The system includes a 3-day sensor that reports glucose measurements every 5 minutes, and can save the data for a review and analysis. A minimum of two blood glucose measurements per day are required for calibration [14]. A similar amperometric device is DexCom STS-7 by DexCom, Inc, which received FDA approval in 2007 for trending and post analysis, and can be used for up to 7 days [9]. The device was

approved to be used with blood glucose strips; hence the users cannot solely rely on the DexCom results. Glucose measurements are taken every 5 minutes, and calibration with a finger stick blood glucose sensor is required every 12 hours.



Figure 1. Picture of FreeStyle Navigator continuous glucose monitoring system. The wireless sensor sends glucose readings to the receiver anywhere within a 10-foot range. Source: Abbott Laboratories (<http://www.freestylenavigator.com/index.htm>)

The latest CGM to be approved by FDA (in 2008) is the FreeStyle Navigator by Abbott Laboratories, shown in Figure 1. This three-electrode amperometric sensor can be inserted under skin for up to 5 days, but glucose is not reported until the first calibration, 10 hours after sensor insertion [15]. Then it requires to be calibrated three more times – 12, 24, and 72 hours after sensor insertion. In this manner, the FreeStyle Navigator needs to be calibrated less frequently when compared to the above mentioned counterparts (Guardian RT and DexCom STS-7). At any rate, all of the above mentioned currently available devices have similar components. The sensors are inserted across the skin using a sharp device to make a cut into the skin and the sharp device is then retracted leaving the sensor in the skin [9, 10]. The invasiveness of such devices together with the requirement of frequent calibrations and frequent replacement is inconvenient, uncomfortable and embarrassing for the end user. Development of a noninvasive glucose sensor can, therefore, greatly facilitate the management of diabetes.

Noninvasive Glucose Sensing

In the last few years, there has been much enthusiasm as well as a strong effort by several companies and universities to quantify blood chemicals, particularly glucose, using various noninvasive optical approaches [16-29]. These include, but are not limited to, near-infrared (NIR) spectroscopy [16-19], polarimetry [23, 25, 30], and Raman spectroscopy [26, 27, 29]. The NIR scatter, Raman scatter, and NIR absorption approaches suffer primarily from a lack of specificity. The NIR scatter approach is especially non-specific to glucose and confounded by changes in indices of refraction

since tissue scattering is caused by a variety of substances and organelles which all have different refractive indices [31]. In case of NIR absorption spectroscopy, the absorption coefficient of glucose in the NIR regime is significantly smaller than that of water due to the large difference in their respective concentrations [32]. The weak glucose absorption bands not only overlap with the stronger absorption bands of water, but also of fats, and other proteins such as hemoglobin. Both NIR scattering and NIR absorption techniques can be confounded by changes in physical and chemical physiological parameters such as changes in blood pressure, temperature, body hydration levels and total protein concentrations in blood [33]. For instance, hyperglycemia can result in vasodilatation, which leads to increase in perfusion [34]. The increase in amount of blood can manifest as increase in light absorption and hence can induce errors in prediction of blood glucose concentration. Similarly, hyperglycemia can potentially lead to accelerated collagen aging [35]. Therefore, light reflected from the skin of a diabetic patient may have different level of intensity in comparison to a healthy subject at equal level of blood glucose concentration.

Likewise, the Raman approach is non-specific, lacks good sensitivity, requires high powers, and suffers from large background autofluorescence of the tissue *in vivo* [32]. Moreover, glucose has inherently small Raman scattering cross section ($5.6 \times 10^{-30} \text{ cm}^2 \text{ molecule}^{-1} \text{ sr}^{-1}$) and hence Raman-based glucose sensors require long acquisition times [36]. Although, a study on the use of Raman spectroscopy for quantitative and noninvasive measurement of glucose was reported successful, it was indicated that there is a need to better understand the scientific basis for the measurement and calibration

processes in order to utilize such technique for practical use [27]. For instance, the instrument wavenumber and intensity stability is critical towards good performance using independent data. Other Raman based techniques such as Raman optical activity and Raman difference spectroscopy have also been applied towards glucose sensing, however, in both the methods, the resultant difference signals are very small and long data acquisition times are required [37, 38].

Recently, several multivariate calibration methods have emerged as powerful tools to complement the spectroscopic techniques [39, 40]. By introducing non-analyte specific variance into the calibration models, several factors that degrade the glucose measurement accuracy of spectroscopic methods have been identified. These include sample variation in absorption and scattering coefficients, tissue autofluorescence, and the physiological time lag between blood and interstitial fluid glucose levels [41-45]. Several correction schemes have been implemented in order to circumvent these factors. Recently proposed models include a mass transfer model based correction scheme that explicitly accounts for glucose kinetics [39], and utilization of both partial least squares (PLS) and support vector regression (SVR) [40] to substantially improve the prediction accuracy of glucose levels.

Polarimetric Glucose Sensing

In comparison to the aforementioned techniques, which usually probe the interstitial fluid and/or blood to ascertain the blood glucose concentration, optical polarimetry has the potential to interrogate the anterior chamber of the eye as a glucose sensing site.

Polarimetric quantification of glucose is based on the phenomenon of optical activity, which is the ability of glucose molecules to rotate the plane of polarization of the transmitted linearly polarized light in direct proportion to the concentration of the glucose. One of the difficulties associated with utilizing polarimetry for glucose sensing *in vivo* is that most of the biological tissues are optically turbid. Polarimetric sensing of glucose in such media thus becomes challenging due to multiple scattering events which scrambles the potentially useful information encoded in the state of polarization of the reflected or transmitted light. A possible way to overcome these problems is to probe the anterior chamber of the eye, since the absorption effects are minimal, loss of polarization information due to scattering effects is insignificant, glucose is the principal chiral component, and a direct correlation exists between blood glucose concentration and that of aqueous humor [46, 47].

The first documented use of polarized light to determine sugar concentration dates back to the late 1800's, where it was used for monitoring industrial sugar production processes [48]. The application of optical polarimetry towards physiologic glucose sensing through the anterior chamber of the eye is more recent and it started with Rabinovitch et al. who were the first to apply polarimetry to the aqueous humor of the eye in order to ascertain blood glucose concentration [49, 50]. Their design was based on an optical feedback system which utilized two Faraday rotators for feedback and compensation. Coté et al. developed a polarimetric scheme based on true phase measurement, demonstrating the potential for millidegree sensitivity in glucose-doped water solutions [51]. Their system employed a rotating linear polarizer as a modulator

and a fixed linear polarizer as an analyzer. Goetz et al. investigated a polarimetric system which used an integrator as the feedback element and were able to measure incremental rotation in a precision rotational mount with microdegree sensitivity [52]. King et al. reported a multispectral polarimetric system in order to account for other optically active components in the aqueous humor, which was based on modulation and compensation via a Pockels cell [53]. Cameron et al. reported a system similar to Rabinovitch, with a digital closed-loop controller which significantly enhanced the stability and repeatability of the system [20]. Chou et al. investigated an amplitude-based optical heterodyne approach which employed a Zeeman laser [54]. In a subsequent work by Coté et al., a dual wavelength system was utilized to minimize the effect of optical confounders in aqueous humor, and potentially, corneal birefringence coupled with motion artifact [55]. They were also able to investigate the glucose transport time delay between blood and aqueous humor of the eye and found that the average transport time lag was measured to be less than 5 minutes [46]. Ansari et al. proposed a polarimetric system which exploited the Brewster's reflection of circularly polarized light off of intra-ocular lens, and were tested the technique on an eye model *in vitro* [56]. Rawer et al. described another Brewster's angle based approach which employed modulation of linearly polarized light in an open-loop system [57, 58]. More recently, Cameron et al. reported on development of a real-time polarimetric glucose sensor which utilized a dedicated birefringence compensator in order to account for corneal birefringence [23].

The aforementioned research indicates that optical polarimetry for monitoring glucose concentration in the aqueous humor of the eye as a potential means of assessing

blood glucose concentration has promise, but the realization of such an approach has been limited by noise from time-varying corneal birefringence due to motion artifact. Consequently, modeling the corneal birefringence of the eye can be critically important toward the understanding of this noise source, and, ultimately, toward the development of a polarimetric glucose monitor. The research presented in this dissertation would address the problems associated with corneal birefringence, and the design and development of this polarimetric glucose monitoring technology would ultimately provide a means for noninvasive measurement of glucose, thereby facilitating increased frequency of the measurement, which will allow the diabetic patient to modify their insulin/glucose regimen in an effort to repress the long term secondary complications of this disease.

CHAPTER II

THEORY

Fundamentals of Light Polarization

Polarized light is essentially light in which the waves are all vibrating in one fixed direction. The electric and magnetic fields associated with the oscillation of these waves are perpendicular to the local direction of propagation i.e. the Poynting vector. In this manner, the associated electromagnetic fields have two degrees of freedom associated with the two directions orthogonal to the direction of propagation. In essence, the state of polarization of light refers to the properties of light within this plane perpendicular to the Poynting vector.

The simplest state of polarization to understand is the linearly polarized light wherein the transverse electric field oscillates in a single direction or plane as a function of both time and space. This state of polarization is usually achieved using a device called polarizer which allows transmission of light in a single plane and (theoretically) blocking out light that exists in other planes. The light leaving the polarizer is referred to as linearly polarized or plane polarized light.

Optical Activity and Polarimetry

While the discovery of optical activity can be traced back to the French physicist Dominique Francois Arago, Louis Pasteur was the first one to realize that molecular symmetry is responsible for the phenomenon of optical activity [59], which is the

rotation of the plane of linearly polarized light passing through a solution of chiral molecules. The remarkable property of chirality is the ability of left-handed and right-handed molecules to rotate light differently, and plays a fundamental role in the chemistry of life.

The equation describing such interaction of light with an optically active compound is given by:

$$\alpha = [\alpha]_{\lambda} C \cdot L \quad (1)$$

where α is the observed rotation, C is the concentration of the optically active sample, and L is the sample path length. In this equation, $[\alpha]$ is the specific rotation which is dependent on the wavelength (λ), temperature and pH. The wavelength dependence is known as optical rotatory dispersion and is further defined using the modified Drude equation for wavelengths away from or between the absorption bands namely [60],

$$[\alpha]_{\lambda} = \frac{k_o}{\lambda^2 - \lambda_o^2} \quad (2)$$

where λ is the wavelength of interest, and k_o is a rotational constant corresponding to the wavelength λ_o of maximal absorption.

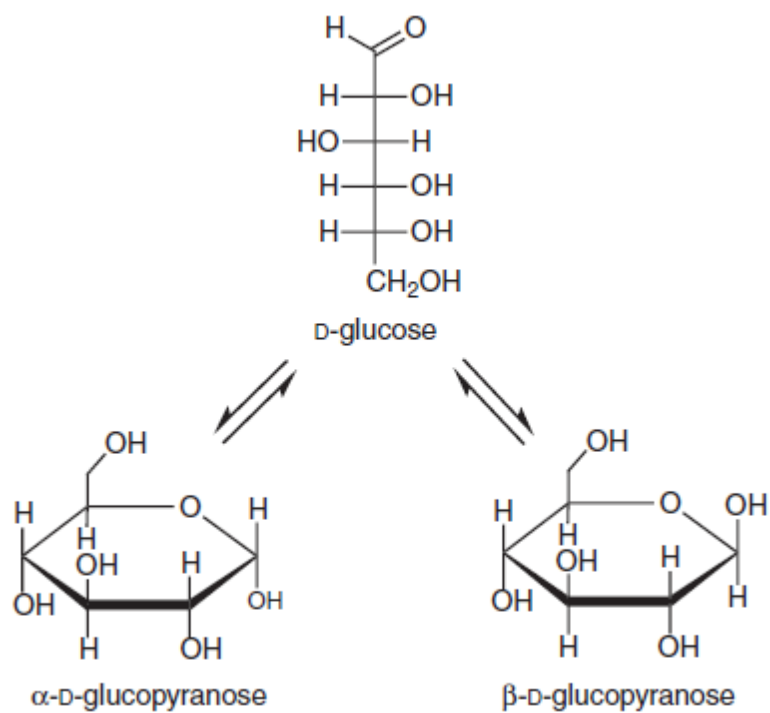


Figure 2. Schematic representation of glucose forms in solution. Fisher (linear) and Haworth (cyclical) projections.

The premise behind the main focus of this research i.e. application of polarimetry for glucose sensing, is based on the optically active nature of glucose molecule. Glucose is one of the most abundant and important sugars in nature. When dissolved in water, the glucose molecule adopts cyclical form(s) as shown in Figure 2. The molecular conformation i.e. α -D-glucose and β -D-glucose are optical isomers known as anomers and differ from each other only in the configuration of the chiral center. After the dissolution, the conversion between α -D-glucose and β -D-glucose is a dynamic process known as *mutarotation* that continues until a thermodynamic equilibrium is reached between the two forms. Individually, the α -D-glucose and β -D-glucose anomers have specific rotation of $+122.2^\circ$ and $+18.7^\circ$, respectively. At equilibrium, the two forms are present in the ratio of 36:64 (α : β) with a net specific rotation value of $+52.6^\circ$. At room temperature and near physiologic pH levels, glucose solution usually reaches equilibrium in about 4 hours.

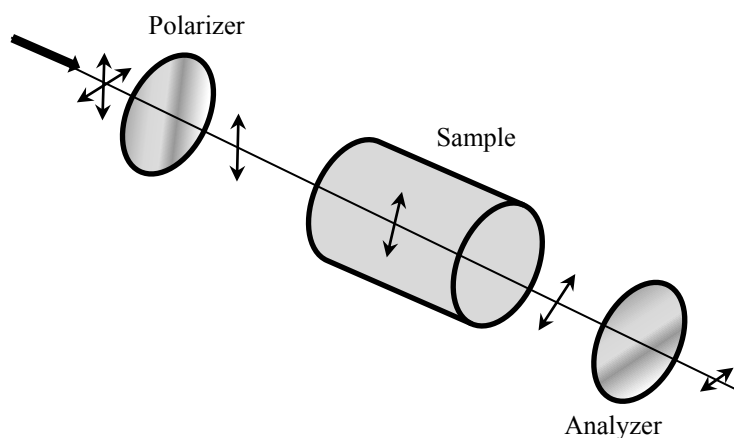


Figure 3. A basic polarimeter comprised of two crossed polarizers with the sample placed in between them.

One of the commonly used devices to measure the rotation due an optically active sample is an optical polarimeter. In its most basic form, it essentially constitutes of two polarizers oriented orthogonally, as shown in Figure 3. After passing the first polarizer, the beam is linearly polarized in the plane of polarization set by that initial polarizer. The second polarizer, known as the analyzer, is usually set at a 90 degree angle with respect to the first polarizer. Therefore, in theory, no light is transmitted in this configuration. If an optically active sample is introduced in between the two polarizers, it rotates the state of linear polarization as it travels through the sample. As indicated in Equation 1, this rotation is directly proportional to the concentration of the sample, and the length of the sample chamber. Now, the light transmitted through the analyzer is proportional to the amount of rotation due to the sample. Consequently, the measured light intensity is a

direct measure of the sample concentration provided the path length and specific rotation of the sample is known.

Anterior Chamber of the Eye

Light enters the eye through the transparent cornea, which also forms the first major refractive component of the eye. It provides both structural and functional integrity while serving as a barrier between the outer environment and inside of the eye. The space between the cornea and the lens tissue constitutes the anterior chamber of the eye which is filled with the fluid *aqueous humor*. As shown in Figure 4, it is formed in a region known as ciliary processes, at an average rate of 2-3 μl per minute [61]. Secretion begins with active transport of sodium ions into the spaces between the epithelial cells. The sodium ions, in turn, pull chloride and bicarbonate ions along with them to maintain electrical neutrality. Then all these ions together cause osmosis of water from the underlying tissue into the same epithelial intercellular spaces, and the resulting solution washed from the spaces onto the surfaces of the ciliary processes. In addition, several nutrients are transported across the epithelium by active transport or facilitated diffusion; these include amino acids, ascorbic acid, and *glucose*. It then flows around the lens through the pupil into the anterior chamber. This flow of aqueous humor also generates an intraocular pressure, which is necessary for the proper contour and optical properties of the imaging optics within the eye. It also nourishes the cornea and the lens, structures that must maintain transparency, and thus cannot depend on blood. Ultimately, the

aqueous humor leaves the anterior chamber of the eye via passive outflow near the *angle* region.

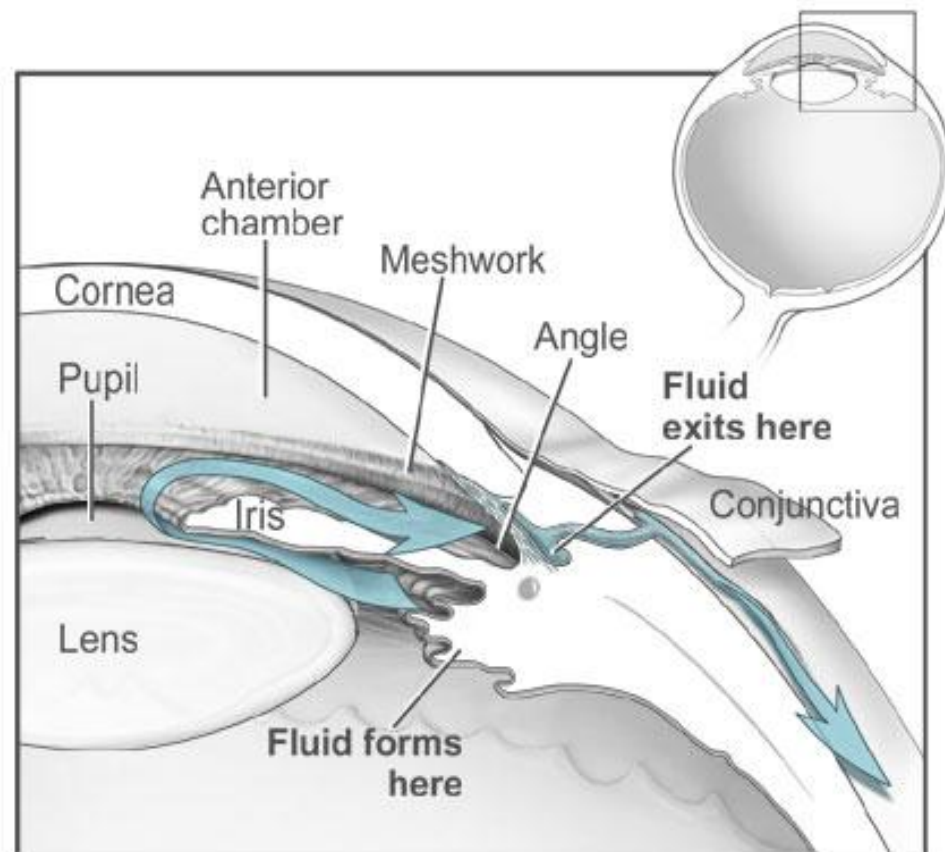


Figure 4. Aqueous humor flows continuously in and out of the anterior chamber and nourishes nearby tissues. The fluid leaves the chamber at the open angle where the cornea and iris meet. The image of the eye shown here is openly available from the National Eye Institute website (<http://www.nei.nih.gov>)

Corneal Birefringence

Birefringence is a property of materials in which atoms are arranged in a regular repetitive array. Such an arrangement can make the material *optically anisotropic* i.e. their optical properties, including the refractive index, are different depending on the direction of propagation of light, and the material is said to be *birefringent* [62]. The direction with the lower value of refractive index is the fast axis, and the difference between the principle refractive indices is a measure of the birefringence, and is usually called the *birefringence*.

The origination of birefringence in cornea is attributed to the retarder like behavior of its collagen lamellae present in the stroma which constitutes more than 90% of the cornea [63], as shown in Figure 5. In humans, the stroma is composed of ~200 stacked lamellae that lie parallel to the surface of the cornea [64]. Each lamella contains narrow and regularly spaced collagen fibrils implanted in a matrix region made up of proteoglycans, inorganic salts, and other soluble proteins. The overall effect of these individual lamellae manifests as corneal birefringence, and is similar to the mechanism of *form* birefringence [65].

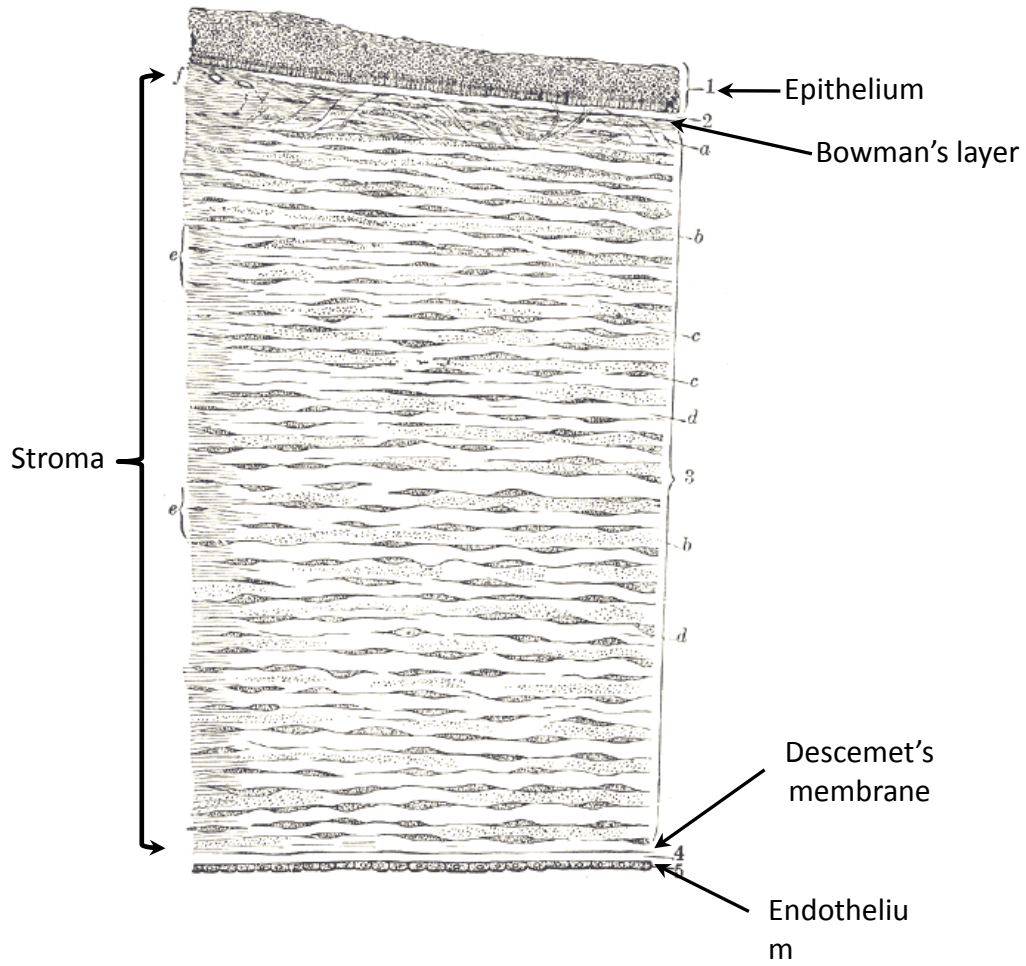


Figure 5. Cross section of the human cornea. Source: H. Gray, *Anatomy of the Human Body*, 1918.

In a healthy eye, the stromal region of the cornea usually scatters less than 10% of the normal transmitted light. This is a remarkable characteristic of cornea given the relative difference in the refractive index between the collagen fibrils and the proteoglycans embedded in the surrounding matrix [66]. One of the proposed mechanisms to address this behavior is that corneal transparency is a consequence of a lattice arrangement of collagen fibrils within stromal lamellas [67]. Such a scheme allows for destructive interference between the light scattered from adjacent fibrils, thereby allowing scattered light to propagate only in the forward direction.

The dependence of corneal transparency on the distribution and size of collagen fibrils is also supported by observations made in swollen corneas. When either corneal surface barrier, endothelial or epithelial, is damaged, the stroma swells up by taking in water. The increase in hydration results in a change in the optimal collagen packing inside the stromal matrix, leading to a loss of transmitted light [68]. For a more technical and mathematical treatment of this behavior, the reader is referred to the original literature [67-70].

CHAPTER III

MODELING OF CORNEAL BIREFRINGENCE^{*†}

Introduction

Several newer technologies for ophthalmic imaging and diagnosis utilize polarized light, thereby making the polarization properties of the ocular tissues an important consideration. For instance, scanning laser polarimetry measures the change in the state of polarization between the incident and reflected beams to measure the birefringence of the retinal nerve fiber layer [71]. Optical coherence tomography uses interferometry to resolve the depth of scattering structures, which requires similar state of polarization in the reference and sample arms to maximize interference signal [72]. Retinal tomography performed with a confocal scanning laser ophthalmoscope utilizes polarizers to accentuate the reflected light from the retinal surface and reduce the noise due to multiply scattered light [73]. In all these aforementioned technologies, unknown and uncontrolled changes in the state of polarization can significantly reduce the device performance. Therefore, any measurement and delineation of polarization properties in a region of eye other than the cornea would require the knowledge and understanding of corneal birefringence. To this end, several theoretical and experimental eye models have been proposed to deal with the extent of corneal birefringence [74-81]. Stanworth and

^{*} Part of this chapter is reprinted from B. H. Malik, and G. L. Coté, "Modeling the corneal birefringence of the eye toward the development of a polarimetric glucose sensor," *J. Biomed. Opt.* 15, 037012 (2010), with kind permission of SPIE.

[†] Part of this chapter is reprinted from B. H. Malik, and G. L. Coté, "Characterizing dual wavelength polarimetry through the eye for monitoring glucose," *Biomed. Opt. Express* 1, 1247-1258 (2010), with kind permission of Optical Society of America.

Naylor proposed that the corneal birefringence for light passing normally through the cornea is small, but increases rapidly with increasing angle of incidence [74]. Bour and Lopes Cardozo proposed a method to measure the retardation as a function of the point of incidence on the pupil plane, and observed that corneal retardation has its slow axis along the tangent to the cornea and that its magnitude increases with increasing eccentricity of the posterior corneal surface [79]. Van Blokland and Verhelst were one of the first to explain the polarization properties of the living human eye with a biaxial model [76]. They also hypothesized that for incidence at higher eccentricity (i.e. near the corneal limbus), a uniaxial model provides good approximation. More recently, Knighton et al. mapped the corneal birefringence using scanning laser polarimetry and reported that a complete description of the corneal birefringence requires the cornea to be treated as a biaxial material [78].

Most of this aforementioned research has been directed towards characterization of polarization properties of the eye with a focus on ophthalmic imaging and diagnosis. Hence, the optical paths usually considered are limited to the region in the anterior chamber which allow for light to pass through the pupil. The commercially available scanning laser polarimeters allow for polarization measurements but are fundamentally limited to macular imaging. Several research groups have reported on the behavior of birefringence in the peripheral regions of cornea [72, 81, 82]. Misson utilized circular polarization biomicroscopy to study the corneal structure and birefringence [82]. Jaronski and Kasprzak devised a phase stepping imaging polarimetry technique to measure the birefringence of human cornea *in vitro*, and concluded that corneal

birefringence increases monotonically in the direction of the corneal periphery [81, 83]. Hitzenberger et al. employed polarization sensitive optical coherence tomography to map the distribution of birefringence at the posterior corneal surface [72]. Their results indicated that birefringence is low for beams incident normal to the corneal surface, and that at oblique angles, measured birefringence increases with deviation from normal incidence. These mentioned reports show the behavior of birefringence in the corneal periphery, and are similar in that the direction of beam incidence is always taken to be normal or near normal to the center of the cornea. We have developed a coupling mechanism to index match the eye and allow light to pass across the anterior chamber of the eye. Explained in detail later, this setup uses mirrors and an inverted tube filled with saline solution as index-matching fluid between air and cornea in order to provide a straight path across the anterior chamber with no coupling through the pupil.

In this chapter, an eye model to investigate the propagation of light and the effect of corneal birefringence on the light transmitted through the anterior chamber is presented. The developed model considers both index-matched and index-unmatched coupling schemes. The knowledge gained from these experiments and modeling can be useful in understanding changes in polarized light as it traverses the anterior chamber of the eye and will provide a framework for building a coupling system toward the development of an optical polarimeter for noninvasive *in vivo* glucose sensing.

Materials and Methods

All optical modeling and calculations were performed in CODE V (Optical Research Associates, Pasadena, CA) optical design software package and MATLAB (The MathWorks, Natick, MA). The CODE V software employs a polarization ray tracing method to solve for the optical path through the optical system, the details of which have been described elsewhere [84]. It has the ability to partition the optical surface into rectangular or circular grid like pattern, where the user has the ability to define the birefringence parameters i.e. the direction of fast axis and the birefringence ($n_e - n_o$, where n_e and n_o are the extraordinary and ordinary refractive indices, respectively) for each individual grid element.

The physical dimensions and parameters of the anterior chamber of the eye were taken from reference [85], in which the corneal surfaces are treated as spherical elements. While a more accurate description of an eye model would include corneal surfaces to be treated as aspherical surfaces, the focus of this study is to model the corneal birefringence and not the exact anatomical dimensions which are important for imaging models. Moreover, it has been shown that an aspherical representation of the corneal surface results in thinner cornea near the limbus when compared to the spherical model [86], which results in a smaller optical path through the cornea and, hence, have a smaller effective birefringence. Thus, we believe that our spherical eye model represents the worst case scenario where the thickness of the cornea in the limbal region is greater than that of an anatomically accurate eye model. As shown in Figure 6, the anterior and posterior sides of the cornea are spheres centered at the optical axis of the eye with radii

of 7.7 mm and 6.8 mm, respectively. Corneal thickness at the center is 0.5 mm, gradually increasing towards the peripheral region of the corneal surface. The refractive indices of cornea and aqueous humor are taken to be 1.376 and 1.336, respectively. As for the medium outside the cornea, we considered two cases: index-matched coupling and index-unmatched coupling.

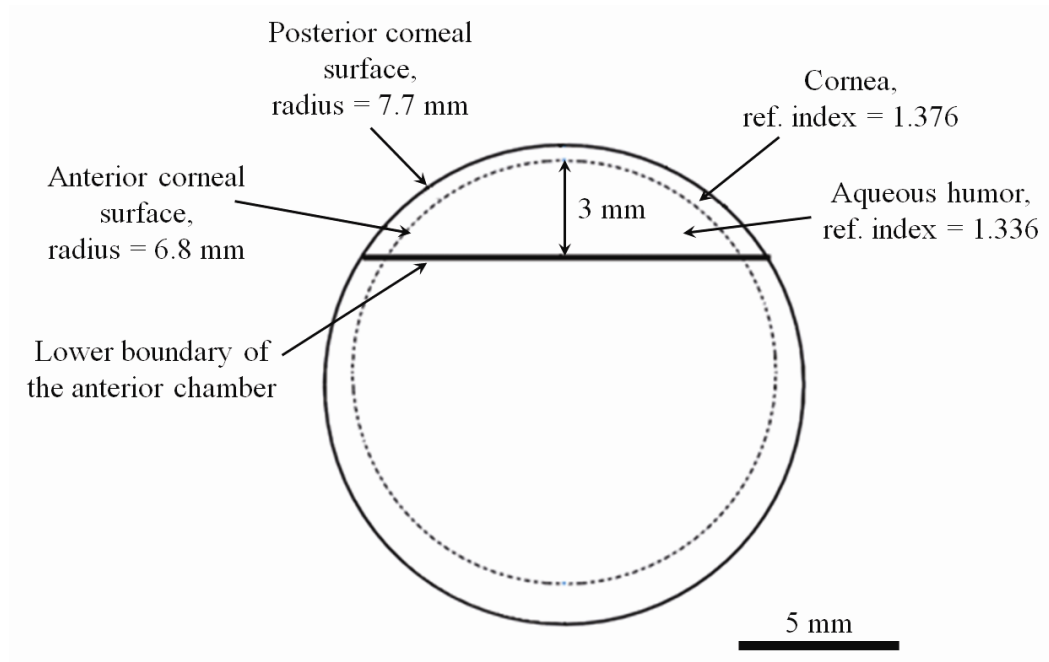


Figure 6. Representative dimensions of the human eye model. The lower boundary of the anterior chamber indicates the position of the pupil and the lens.

A local x-y-z coordinate system is defined at any arbitrary point on the posterior corneal surface such that the tangential plane at that point coincides with the x-y plane, then the fast axis points in the z- direction, as illustrated in Figure 7. Hence, the electric field of a light ray incident normal to the corneal surface only experiences n_x and n_y . In general, not all incident light is normal to the cornea, and therefore, the corresponding electric field vector experiences n_x , n_y and n_z . Thus, a biaxial model can better explain the corneal birefringence in which each of the principle coordinate axis is associated with a different refractive index. However, according to Van Blokland and Verhelst, $n_z - n_y$ is about 10 times larger than $n_y - n_x$ [76]. Therefore, at larger oblique incident angles (explained later for our coupling scheme), a large component of the electric field vector lies along the z- axis and a uniaxial model will give a good approximation. We modeled our eye as a bent uniaxial slab where at each point the fast axis coincides with the direction of local normal, and a maximum birefringence of 0.00159 as calculated by Van Blokland and Verhelst [76].

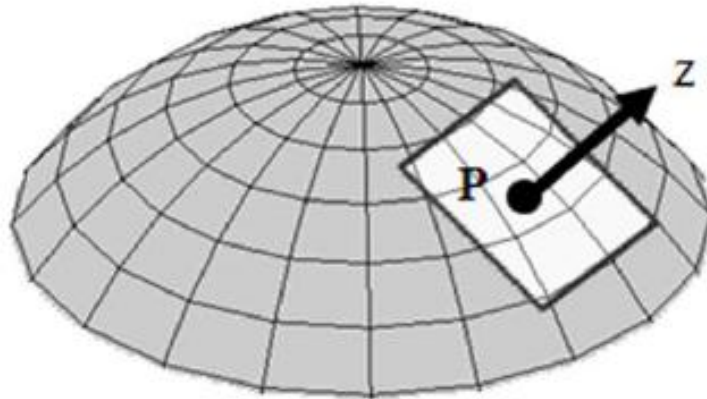


Figure 7. Local Cartesian coordinate system at an arbitrary point P on the posterior corneal surface. The system is aligned such that the z-axis is coincident with the local normal, and the x-y plane represents the tangential plane at the point P.

Index-matched Coupling of Light

The environment outside the posterior corneal surface was assumed to be buffered aqueous-saline solution ($n = 1.33$) for index matching. As shown in Figure 8, incident light was tangentially coupled to the anterior chamber of the eye. The advantage of using an index-matching solution is to minimize the change in the angle of refraction at the interface of the aqueous solution and the posterior cornea. The change in the refractive index between saline solution and cornea is on the order of 10^{-2} . Similarly, the same order of difference exists between refractive indices of cornea and aqueous humor, and hence the deviation in beam angle on entering and leaving the eye is minimized. Moreover, a direct consequence of this reduced refraction is that the output beam shape and size are maintained along with negligible change in the beam divergence.

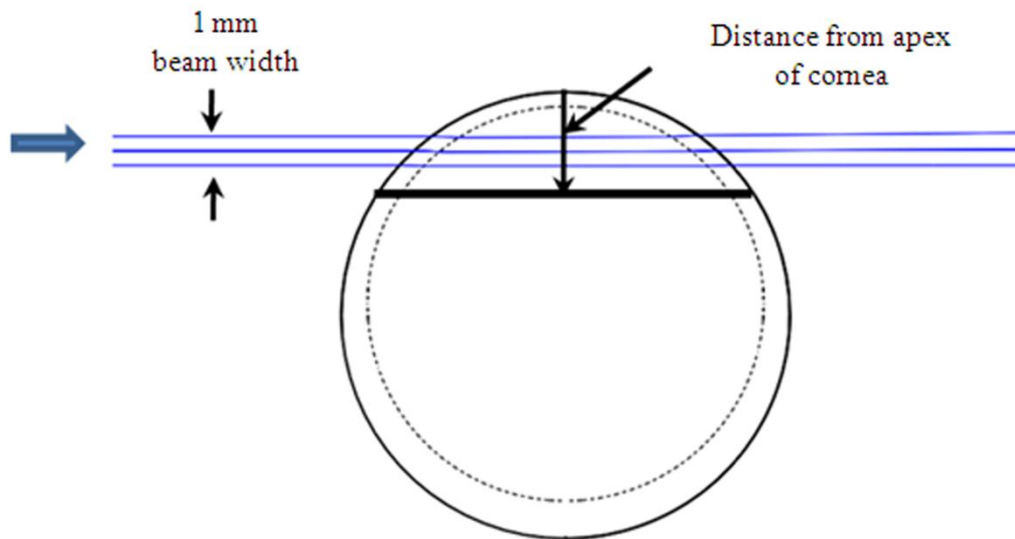


Figure 8. Optical path through the anterior chamber of the eye. Note that the beam passes effectively straight through the chamber due to the assumption that the eye is index matched.

Due to the curvature of the cornea, the optical path length through the cornea, and thereby the retardance, varies greatly depending on both the angle and point of incidence. In order to analyze this variation in our eye model, we initially assumed a circular 1-mm-diameter light beam at 635-nm wavelength, and later used a 532-nm wavelength beam for comparison. As a result, in order to couple the full area of the beam, the top most point of incidence was chosen to be 0.5 mm (i.e. the radius of the beam) below the interior apex of the cornea. Similarly, the lowest point of incidence was chosen to be 0.5 mm above the limbus. The polarization vector of light beam propagation model was chosen to be at 45 degrees with the vertical axis.

Index-unmatched Coupling of Light

The most noteworthy difference in coupling of light through the anterior chamber of the eye compared to the index-matched environment is that the incident light must enter the eye at a relatively larger glancing angle with respect to the posterior corneal surface, as shown in Figure 9. Without any index matching, both the beam position and angle for which the light beam of a given diameter and shape can be coupled through the anterior chamber are limited. Similar to the case of index matched coupling, we assumed two circular beams at two wavelengths (532-nm and 633-nm) with diameter of 1 mm. Both the beam position and angle of incidence were varied to explore the behavior of corneal birefringence and to find a region of minimal change in its effect, if any.

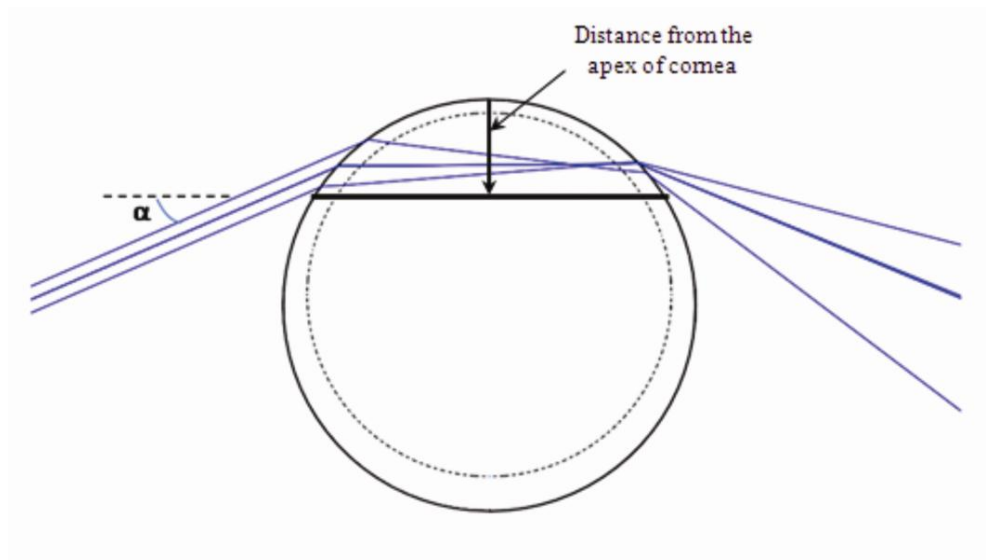


Figure 9. Optical path through the anterior chamber of the eye for unmatched refractive indices. The angle of incidence, α , is measured from the horizontal. Note that light has to be incident at a relatively glancing angle with respect to the posterior corneal surface in order for the beam to exit the anterior chamber through the cornea. There is no visible difference (on the current scale) between the optical paths taken by the two beams at different wavelengths, and hence, a single beam path is shown.

Experimental Setup to Measure the Effect of Corneal Birefringence

The experimental measurements of the effect of birefringence were performed on three New Zealand White (NZW) rabbits' eyes. All experiments were performed on eyes < 4 hours postmortem, and the corneas were visibly transparent before, during, and after the polarimetric measurements. The plane of incidence was taken to be along the nasal meridian and the point of incidence was at the nasal side of the eye for all instances. As illustrated in Figure 10, the optical sources were two lasers: a 633-nm He-Ne module (JDS Uniphase Corp., Milpitas, CA) and a 532-nm diode-pumped solid-state laser module emitting at 1 mW and 4 mW, respectively. Both beams were made coincident using mirrors on flip mounts (Thorlabs, Newton, NJ) and the output light was polarized (100,000:1) at 45° by employing a Glan-Thompson linear polarizer (Newport, Irvine, CA). The combined beam was then passed through the anterior chamber of the eye. In order to change the beam incidence position and angle, the eye stage was mounted on a combined translational (Thorlabs, Newton, NJ) and rotational mount (Newport, Irvine, CA). The optical train terminated in the input facet of a rotating waveplate-based polarimeter (Thorlabs, Newton, NJ) which was connected to a personal computer for real-time state-of-polarization measurements.

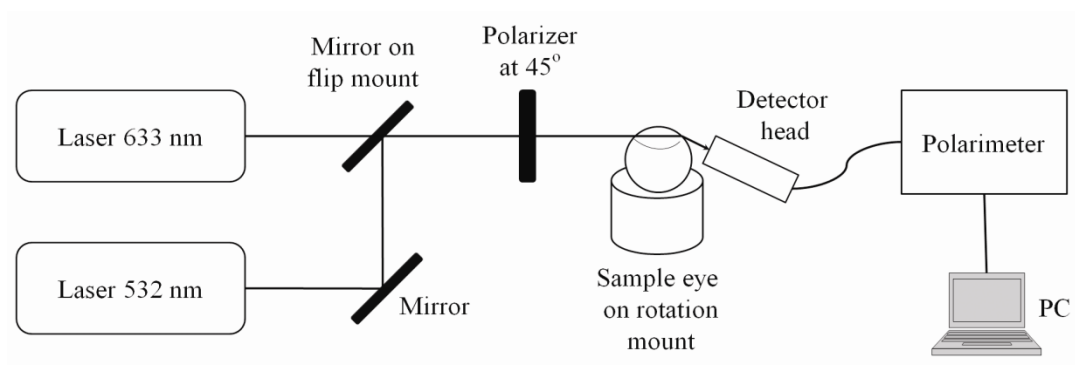


Figure 10. Optical configuration for experimental measurement of corneal birefringence. Note that one of the mirrors was placed on a flip mount in order to couple either wavelength at a time.

Results and Discussion

Index-matched Coupling of Light

To analyze the change in major axis for elliptically polarized output light due to the corneal birefringence, the beam position was varied from top to bottom of the anterior chamber in 0.1-mm-intervals. The glucose concentration in the aqueous humor was assumed to be zero and hence it does not contribute to the rotation of light. As shown in Figure 11, there is a sharp change in the angle near the apical region and the angle of major axis changes by almost 90 degrees across the circular state of polarization. It can be seen that the change in the perceived angle of polarization is much smaller for a beam position below 1 mm and is minimal around 1.6 mm below the apex of cornea which is near the center of the available probing line of incidence. Thus, the effect of corneal birefringence can potentially be minimized for a beam incident at roughly 1.6 mm below the apex of the eye. This can also be seen in Figure 12 which shows the change in the state of polarization as a function of beam position. While the ratio of major-to-minor axis of the ellipse changes in the center region around 1.6 mm below the apex of the eye, the orientation of major axis stays relatively constant.

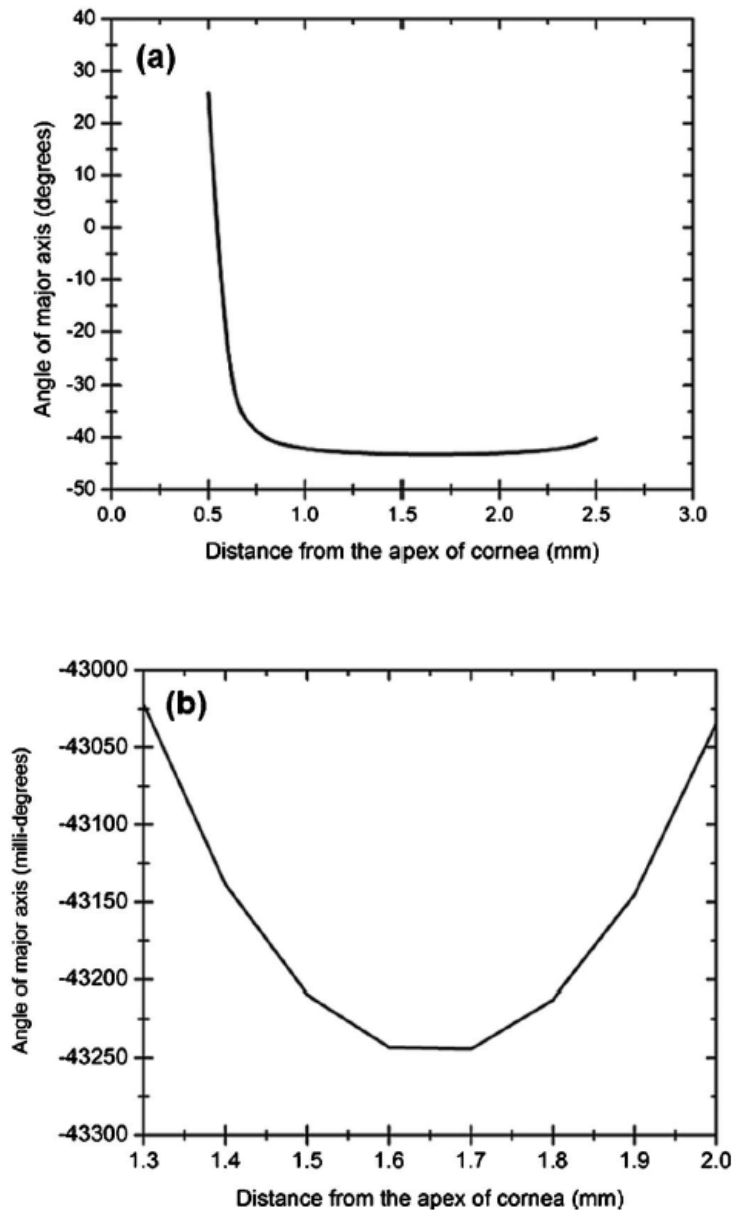


Figure 11. (a) Angle of major axis of the output beam polarization ellipse as a function of distance from the apex of the cornea. Note that after a rapid change in the orientation of major axis near the apex, the variation is much smaller for beam positions below 1 mm. (b) Angle of major axis as a function of distance from apex of cornea—zoom-in view of the 1.3-mm to 2.0-mm region. Note that a shift in the beam position from 1.5 to 1.4 mm produces a net rotation of ~ 71 millidegrees due to change in corneal birefringence.

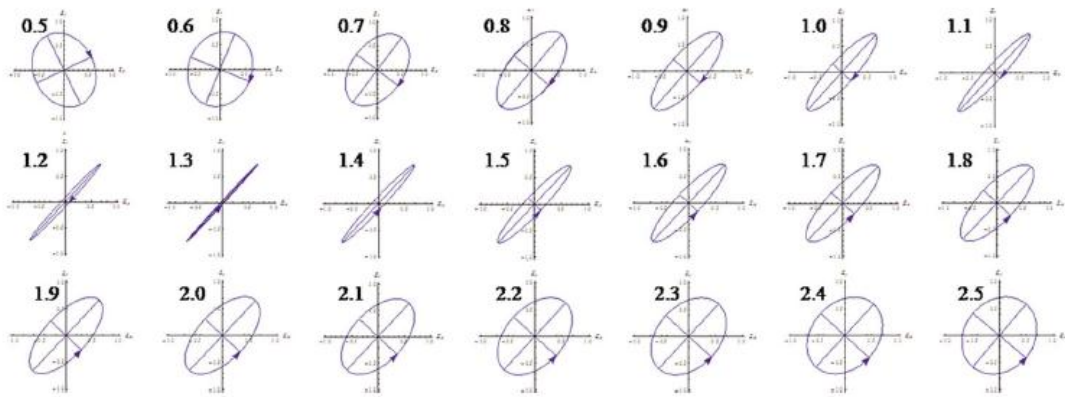


Figure 12. Variation in state of polarization as a function of distance from the corneal apex. Note that although the eccentricity of the ellipse varies near the center of the eye, the major axis orientation stays relatively unchanged.

Apart from change due to birefringence, it is known that the optical path length through the aqueous humor of the eye and the glucose concentration itself would also change the measured rotation. Moreover, the path length is a function of beam position on the posterior corneal surface and that the glucose could vary across the physiologic range. Therefore, the effect of change in both of these parameters on the rotation should be compared to the changes observed due to the effect of corneal birefringence. The change in optical path length as a function of the distance from the apex to the limbus is plotted in Figure 13a, and then converted to a change in rotation as plotted in Figure 13b using equation 1, and assuming a normal 100 mg/dL glucose concentration. The plot in Figure 14 shows the change in rotation as a function of glucose concentration across the 0-600 mg/dL range for a beam position of 1.6 mm below the apex which corresponds to optical path length of 8.82 mm. We also took into account the effect of glucose concentration dependent change in refractive index and, thereby, on the optical path length. The increase in the refractive index of an aqueous solution of glucose with increasing glucose concentration is 2.5×10^{-5} /mM glucose (or 1.39×10^{-6} /mg/dL) [87]. This amounts to a change in refractive index of 8.34×10^{-4} across the glucose concentration range of 0 to 600 mg/dL. Such a small change in refractive index has negligible effect on beam path deviation across the physical path length in the anterior chamber of the eye.

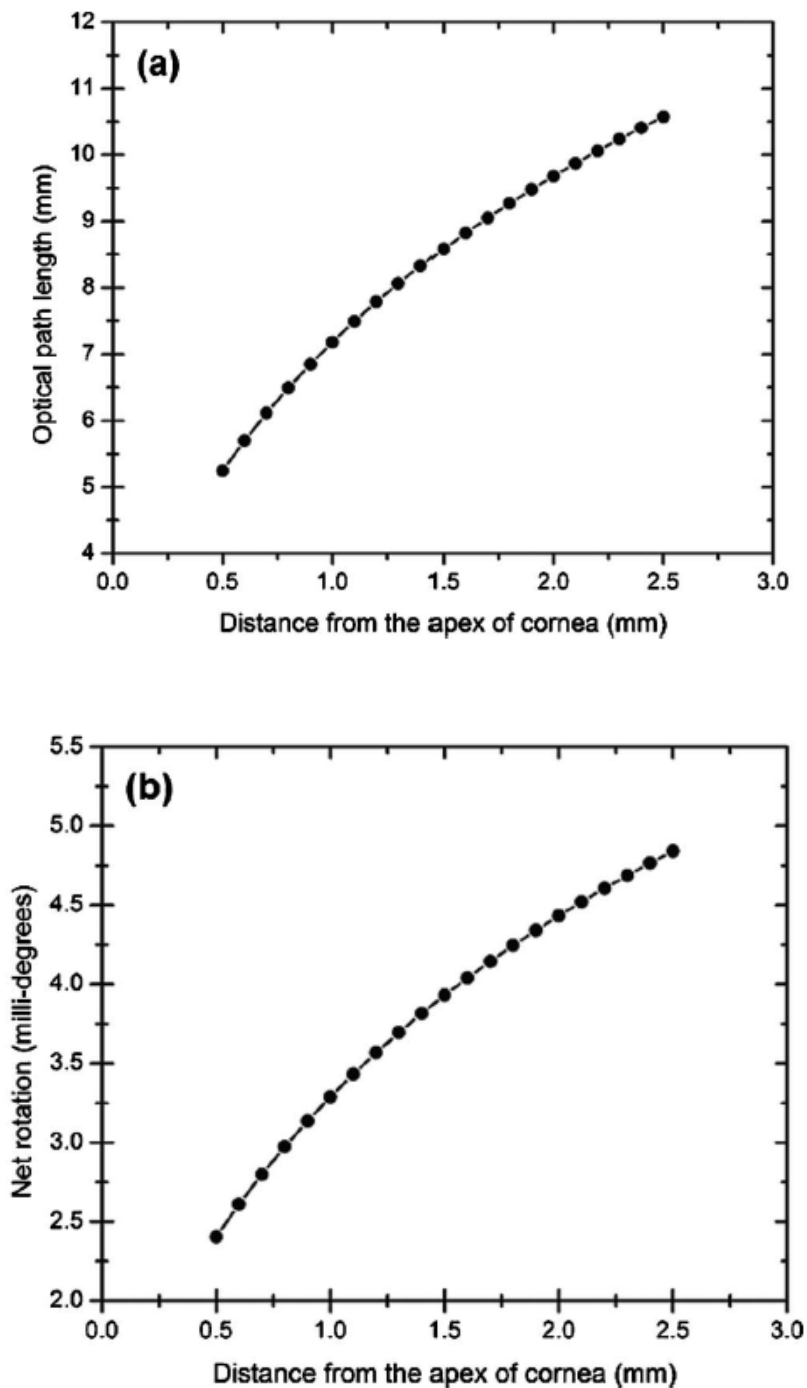


Figure 13. (a) Change in optical path length through the aqueous humor as a function of distance from the apex of the cornea, and (b) corresponding net rotation in angle of polarization vector as a function of distance from the apex of the cornea.

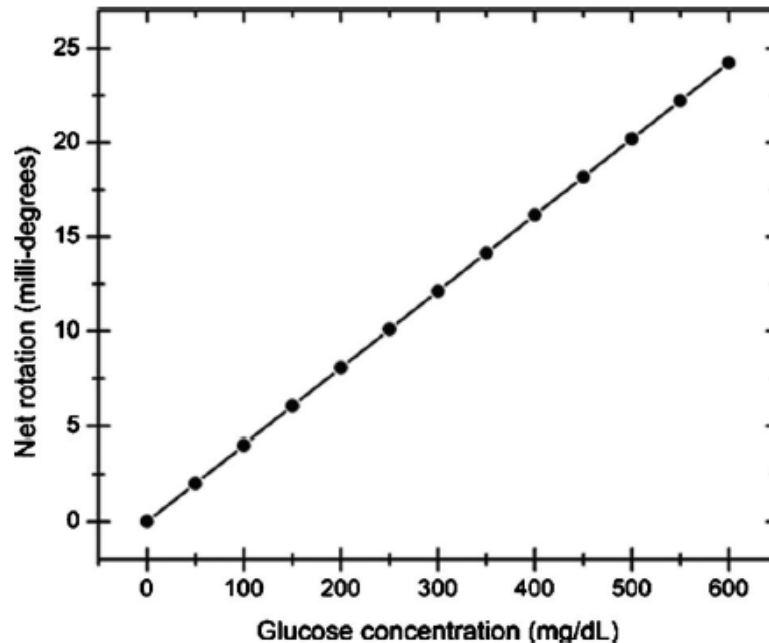


Figure 14. Net rotation in the angle of polarization vector as a function of glucose concentration. The point of incidence is taken to be 1.6 mm below the corneal apex, which corresponds to an optical path length of 8.82 mm through the aqueous humor.

It is clear from Figures 13-14 that for any given change in beam position such as that due to motion artifact in the eye, the change in net rotation due to corneal birefringence is at least an order of magnitude larger than the effect of changes in optical path difference and aqueous humor glucose concentration. For instance, as depicted in Figure 4b, if the laser beam incidence shifts from 1.5 mm to 1.4 mm due to motion artifact, the change in the polarization vector due to corneal birefringence would be ~ 70 millidegrees. In comparison, the corresponding change in optical path difference produces a net rotation of only 0.12 millidegree. Similarly, a change in glucose

concentration by $\pm 10\text{mg/dL}$, which is the current experimental error in glucose estimation [20, 25], changes the net rotation of polarization vector by ± 0.4 millidegree. This analysis clearly demonstrates that even in the most stable region, the time varying corneal birefringence is the most significant noise source in the sample and a major limitation preventing realization of an optical polarimetric approach to ascertain aqueous humor glucose concentrations *in vivo*.

As explained later in chapter 4, a possible method proposed by our group to reduce and potentially eliminate the effect of corneal birefringence is to utilize a multispectral scheme [25]. This is done by multiple-linear regression (MLR) analysis which is analogous to scaled subtraction. By utilizing at least two wavelengths away from or between the absorption bands for glucose, MLR can accommodate the contribution of birefringence to the total rotation of the state of polarization and equation 2 can be used to predict glucose. One of the assumptions for such an analysis is that the motion artifact is wavelength relatively independent in the range of motion. To validate this assumption, we utilize a second wavelength away from the glucose absorption band at 532 nm and examine the perceived angle of polarization axis due to corneal birefringence with respect to that of 635 nm wavelength. Figure 15 shows the plot of major axes of elliptically polarized output beams at both the wavelengths. It can be seen that after a rapid change near the apical region of the eye, the major axes orientations remains relatively unchanged and close to each other, especially between 1.4 mm and 1.8 mm. This observation leads to two important advantages. Firstly, for any of the two wavelengths, coupling of light at just under the center of the cornea leads to minimum

change in state of output polarization due to motion artifact. Secondly, the major axis orientations of both the wavelengths have similar magnitude, a direct consequence of which is that a dual-wavelength optical polarimeter can be utilized to reduce the sample noise associated with motion artifact.

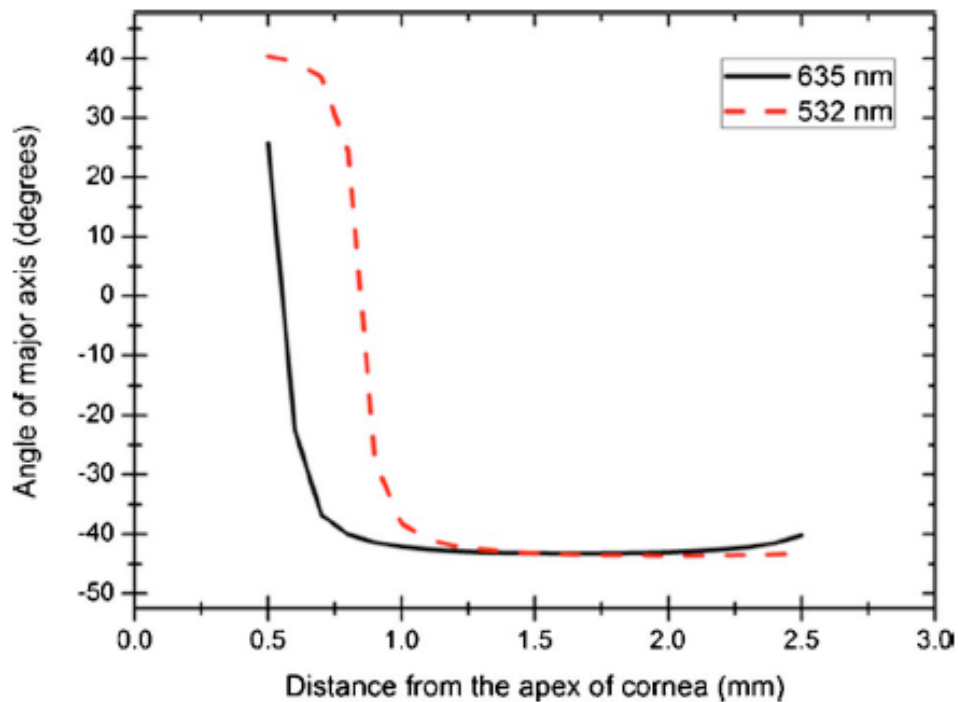


Figure 15. Angle of major axes for wavelengths of 635 (solid line) and 532 nm (dashed line) as a function of distance from the apex of the cornea. Note that after a rapid change in the major axes orientations near the apex, the variation is much smaller for beam positions below 1 mm, and is of similar magnitude.

Index-unmatched Coupling of Light

In the case of index-unmatched coupling of light through the eye, there is a limited range of incident angles for which the full width of the beam can be coupled in-and-out of the anterior chamber. Also, regardless of the angle of incidence, there is range of beam position (measured as the distance from corneal apex) for which the full beam is able to leave the anterior chamber. For the dimensions and beam size used in our model, this range of input was calculated to be from 1.6 mm to 2.5 mm below the corneal apex. For any possible combination of incident beam position and angle, the output beam is divergent. Based on this information a total of three different beam positions – 1.6 mm, 2.0 mm, and 2.5 mm below apex – were selected and the possible ranges of incident angles for which the full width of the beam can leave the eye were probed. The corresponding data values are plotted in Figure 16, which shows that the largest and shortest range of incident angles can be attributed to the beam positions of 2.5 mm and 1.6 mm below the corneal apex, respectively.

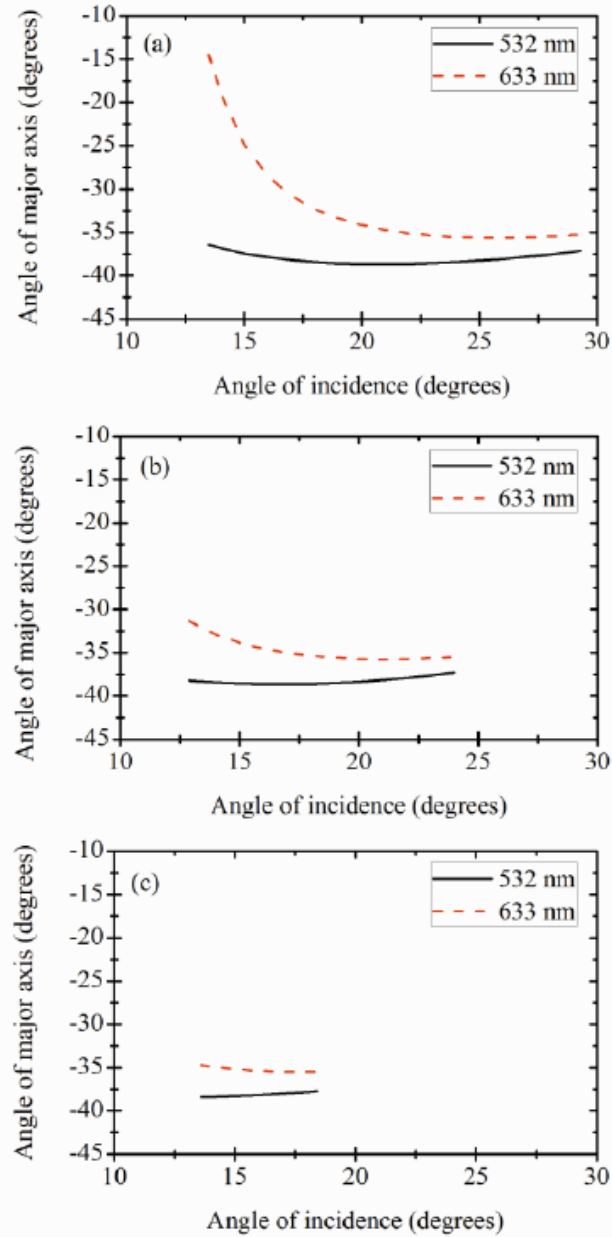


Figure 16. Angle of major axis of polarization ellipse as a function of angle of incidence for beam position at (a) 2.5 mm, (b) 2.0 mm, and (c) 1.6 mm below the corneal apex. . Note that the change in the angle of major axis of the output beam (i.e. the y-axis) represents the effect of corneal birefringence only. The angles are calculated assuming only aqueous humor without glucose or any other optical rotatory components present in the anterior chamber of eye.

It should be noted that, although the overall range of major axis angles associated with beam positions of 2.5 mm and 2.0 mm show larger deviations in due to corneal birefringence, there is a region in which this deviation is minimized but only when larger angles of incidence are used. In comparison, the full available range of angles for a beam position of 1.6 mm below the apex shows minimal change in perceived major axis angle of the polarization vector for smaller incidence angles. In addition, it can be seen in Figures 17b and 17c that for light coupled at beam positions of 2.5 mm and 2.0 mm below apex, and at angles which show minimal change in the output beam's major axis, the beam tends to focus more towards the center of the anterior chamber and away from the opposite anterior corneal surface. Consequently, the beam at the exit is more divergent compared to that of incidence at 1.6 mm (Figure 17a), in which the focal point is near to or in the cornea. Therefore, the beam incidence at 1.6 mm below the apex would allow for a smaller incident angle and thus relatively less complicated coupling when compared to incidence at 2.0 mm and 2.5 mm below the apex. In particular, the position of eye with respect to the nasal bone may limit the range of incident angles. For instance, if the coupling is performed by placing a mirror in between the eye and the nasal bone then it may potentially be simpler to couple light at smaller incident angles. Therefore, the beam incidence at 1.6 mm below the apex appears to be the optimal position to minimize the effect of both corneal birefringence and the curvature of the eye despite a short range of available incident angles.

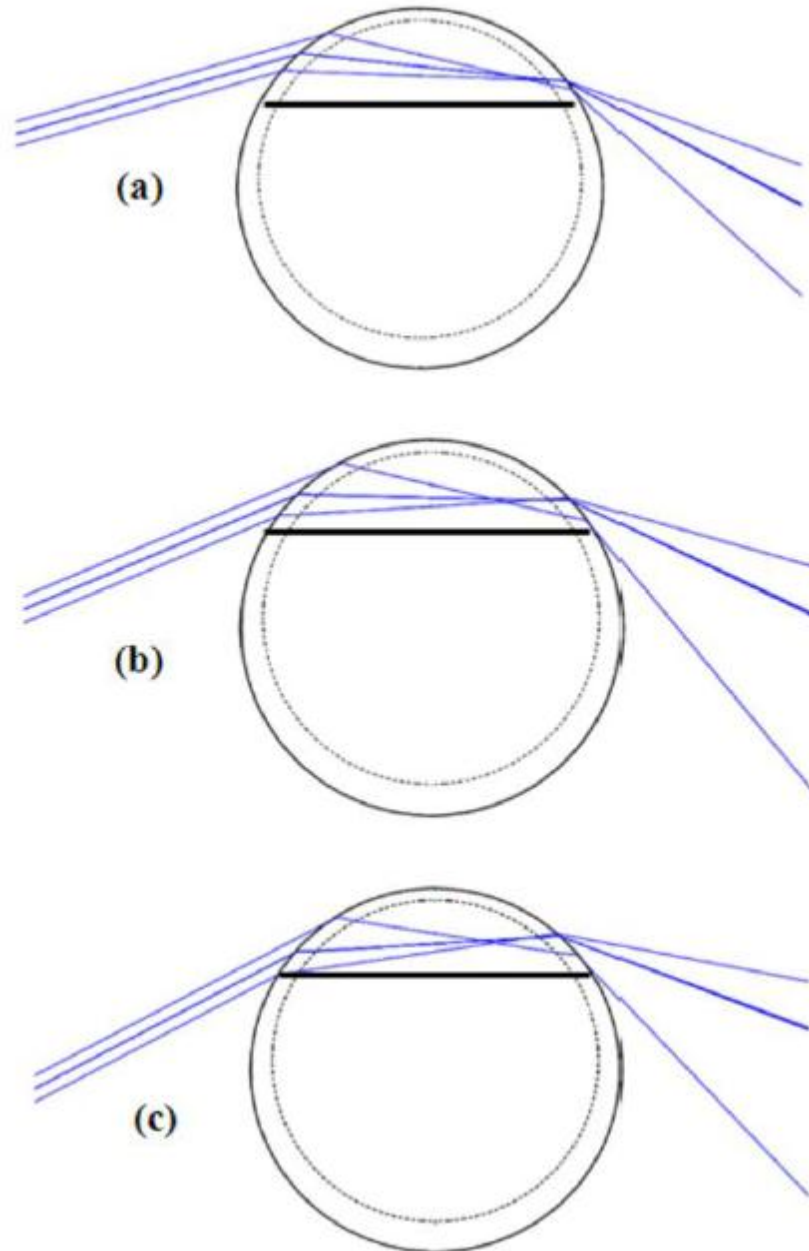


Figure 17. Optical path through the anterior chamber of the eye for beam position and angle of incidence at (a) 1.6 mm and 16° , (b) 2.0 mm and 23° , and (c) 2.5 mm and 28° , respectively.

It should be noted that even in the most stable range of change of angle of major axis, a small change in the incidence angle rotates the output polarization vector by a magnitude much larger than that of due to change in optical path length through the anterior chamber and/or glucose concentration. For example, as mentioned above, a maximum change in optical path length through the aqueous humor contributes to a net change of ~ 2.5 millidegrees in the angle of polarization vector. Similarly, a 10 mg/dL change in glucose concentration produces a net change of ~ 0.4 millidegrees for light at 633-nm wavelength. In comparison, if the incidence angle changes from 15° to 16° due to motion artifact, the rotation in polarization vector due to corneal birefringence is ~ 200 millidegrees. This observation demonstrates that time varying corneal birefringence due to motion artifact is a major source of noise that needs to be accounted for in order to realize polarimetric quantification of glucose *in vivo*.

That being said, in the case of a change in incidence angle due to motion artifact, the MLR analysis would benefit from a linear relationship between the change of angle of major axes for the two wavelengths as a function of incidence angle. MLR analysis of the respective data points in Figure 16c demonstrates a linear relationship with R^2 -value of 0.9999 across the available range of incidence angles. Hence, the rotation in major axis of the state of polarization due to a change in angle of incidence can potentially be accommodated using MLR analysis, and as a result, this modeling indicates that a dual-wavelength optical polarimeter can potentially be utilized to reduce the contribution of sample noise related with motion artifact.

Experimental Measurement of the Effect of Corneal Birefringence

To establish the validity of our eye model, experimental measurements were performed. Birefringence measurements were performed on NZW rabbits' eyes ($n = 3$). The angle of incidence was set at approximately 15° with the beam position near or at 1.6 mm. The output beam casts a coma-like diverging pattern making it complicated to collect the full area of the beam without using collection optics. To overcome this problem, the detector head of the polarimeter unit was placed very close to the beam exiting the corneal surface. The relatively large size of detector head was also useful in maximizing beam collection.

The measured individual and mean angle of the major axes is plotted as a function of wavelength in Figure 18. Overall, the effect of corneal birefringence was observed to be somewhat consistent between the three eyes. It should be noted that although the mean measured value for 532 nm wavelength agrees with that of our model, the major axis angle for 633 nm wavelength showed a slight deviation when compared to the predicted value. It should be noted that the alignment to overlap the beams was done manually and, as explained below, this small overlap mismatch may be responsible for generating this deviation from the modeled values. The relative consistency between eyes can be useful towards establishing a general calibration model for a dual wavelength optical polarimeter; nonetheless, as long as the difference within an eye is constant this should be good enough for compensation of corneal birefringence within that eye.

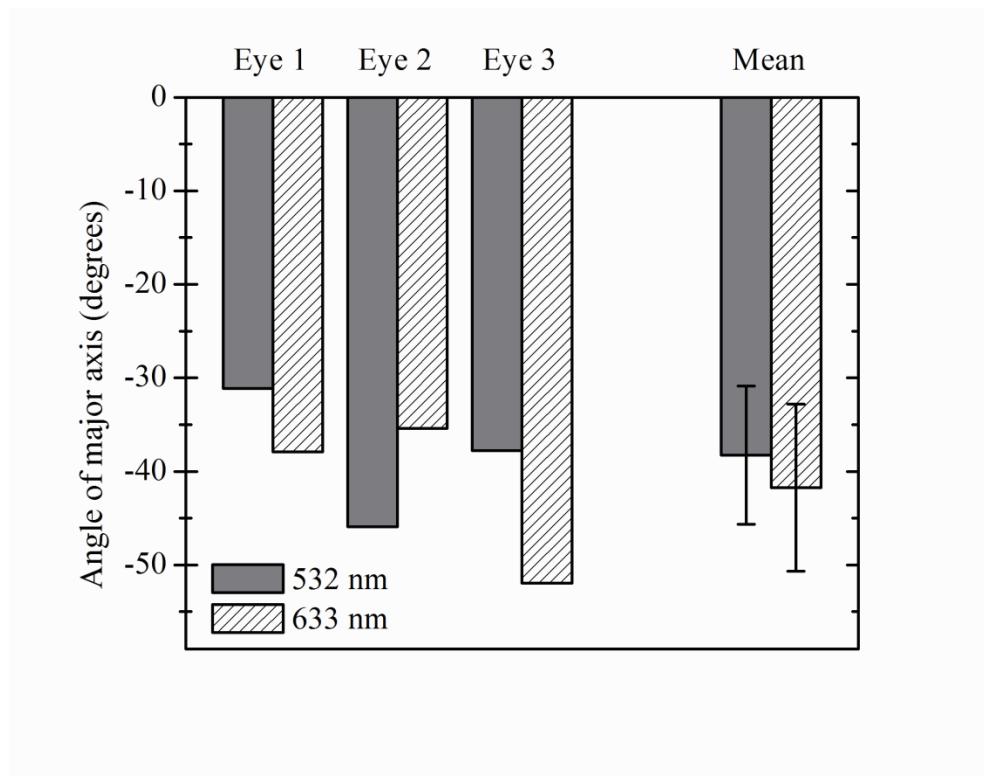


Figure 18. Inter-eye variation of measured angle of major axis of polarization ellipse as a function of wavelength. The data points include measurements for three individual eyes and their overall average.

The variation in the effect of corneal birefringence as a function of change in the angle of incidence within a single eye was measured. Measurements taken at an angle of incidence of 15° , 16.5° and 18° , plotted in Figure 19, show the variation in the measured angle of the major axis as a function of incidence angle. It can be seen that there is a discrepancy in measured values when compared to the eye model. This can be attributed to the differences in the distribution of birefringence in the cornea of rabbits' and human eyes. Such a comparison has been previously reported by Wang and Bettelheim, who investigated the corneal birefringence in several species [88]. The maps of birefringence isochores in the human eye show highly centro-symmetrical behavior which is similar to that of our eye model. In comparison, the birefringence isochore map of the rabbit cornea is relatively anisotropic. As a result, even a small deviation from the nasal meridian can cause inconsistency between the modeled and experimental observations. It was noted, however, that the net difference between the measured values at respective wavelengths is relatively unchanged. Thus, the above mentioned MLR analysis can potentially account for these changes, consequently, showing the potential of a multispectral polarimetric approach towards reducing the effect of corneal birefringence and allowing quantification of glucose in the anterior chamber of the eye.

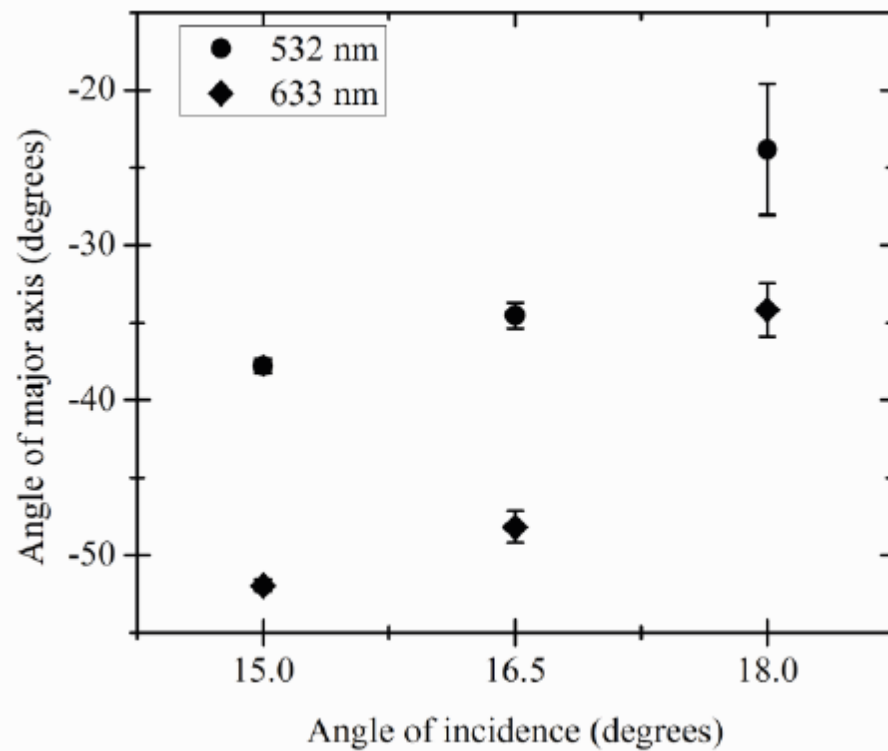


Figure 19. Intra-eye variation of measured angle of major axis of polarization ellipse as a function of wavelength and angle of incidence. Note that the angle of major axis changes significantly with change in angle of incidence, but the net change between the data points for respective wavelengths is relatively constant.

The variation between the measured values shown in Figures 18 and 19 and values generated from the model can also be attributed to experimental limitations such as the light beam positioning, which was done manually by visual inspection. Hence, it is possible that the incident spot was not completely coincident with the desired position of 1.6 mm below the apex and/or at the center with respect to the x-plane. This can have a considerable effect on the effective corneal birefringence experienced by the light beam. For example, de-centering of 633-nm beam position by a millimeter in our model would change the output beam's angle of major axis by magnitude of $\sim 16^\circ$. Specifically, a +1 mm horizontal change from the center placement changes the major axis angle to -51.4° compared to the previous value of -35.2° . This further highlights the significance of time varying corneal birefringence due to motion artifact as a noise source, where such a small deviation from the theoretically modeled values can lead to a substantial change in experimental observations. Moreover, postmortem artifacts like stromal edema and corneal autolysis can potentially change the tissue ultrastructure over time thereby changing the effective corneal birefringence properties, which may further increase the discrepancy between the modeled and measured data. However, even though the absolute values are different for the model versus the experiment, the relative values for each wavelength and difference between wavelengths is relatively constant showing the potential for the dual wavelength approach to compensate for these changes, which can be present due to motion artifact.

CHAPTER IV

POLARIMETRIC GLUCOSE SENSING[‡]

Introduction

Polarimeters determine the polarization state of a beam of light or some of its polarization characteristics, which may vary from simply determining the plane of oscillation for a linearly polarized beam, to as complex as the complete polarization parameters of an elliptically polarized beam. A polarimeter utilizes a set of polarization elements and components placed in the path of the light. As mentioned earlier, the most basic form of polarimeter consists of essentially two crossed polarizers. Such a simple setup is adequate if the optical rotation to be measured is on the orders of several degrees i.e. samples with high concentration and/or long path lengths.

In order to provide very small angle measurements with high measurement sensitivity, polarimeters often employ mechanisms to modulate the plane of polarization of the incident field about the optical axis. Along with an analyzer, a modulator can be used to both switch the polarized intensity between two orientations on a single detector, or exchange between two detectors. If the modulation is done rapidly enough, this technique can mitigate the effects of noise related to random events and temperature-dependent drift, which plague low-frequency measurements.

[‡] Part of this chapter is reprinted from B. H. Malik, and G. L. Coté, "Real-time, closed-loop dual-wavelength optical polarimetry for glucose monitoring," *J. Biomed. Opt.* 15, 017002 (2010), with kind permission of SPIE.

In earlier designs, polarization modulation for polarimeters was accomplished by physical rotation of a polarizer about the optical axis [51] or rotation of a birefringent waveplate [89]. Such modulation schemes often tend to employ bulky and complex mechanisms which are subject to failure with repeated use. More recent methods utilize electro-optic, magneto-optic or photoelastic effects to modulate the state of polarization of light [90]. The polarimeter designed for this research employs a magneto-optic modulator for polarization modulation of light, which is based on the Faraday effect [62] and is described in detail below. The system also utilizes Faraday rotation to compensate for the rotation due to glucose, which serves as a mechanism to provide feedback control, another fundamental aspect of this research.

In this chapter, we describe the development of a dual wavelength optical polarimeter utilizing real-time closed-loop feedback control to ultimately overcome corneal birefringence. At first, the system was characterized *in vitro* using a birefringent plastic cuvette, and the performance of the system is measured against an open-loop system. Later, the sample cuvette was replaced by eye phantoms, which include a plastic eye model (*in vitro*) and isolated corneas from New Zealand White (NZW) rabbits (*ex vivo*). Finally, the system was applied *in vivo* on anesthetized NZW rabbits.

Materials and Methods

Dual Wavelength Polarimeter

The optical configuration of our dual wavelength system is based on a set of crossed polarizers, a modulating Faraday rotator, and dual Faraday compensators used for

closing the loop. As depicted in Figure 20, the optical sources are two laser diode modules (Power Technology Inc.) at wavelengths of 635 nm and 830 nm emitting at 7 mW and 20 mW, respectively. The 830-nm laser was later replaced by a 532-nm diode-pumped solid-state laser. The output light is polarized (1:100,000) by employing Glan-Thompson linear polarizers (Newport). Both the beams then pass through respective in-house built Faraday rotators which act as rotation compensators and are present only for closed-loop operation. The design and working principle of these active devices are described in detail in the following section. The two beams are then made coincident using a beam splitter/combiner (Optosigma Corp.). The polarization vector is modulated using a modulating Faraday rotator at 1.09 kHz with modulation depth of $\sim \pm 1$ degree. The light then passes through a moving birefringent sample, a moving plastic cuvette with glucose doped water solutions in the physiological range of 0 to 600 mg/dl. For *ex vivo* experiments, the cuvette is later replaced by the eye respective eye phantoms. The motion of the sample is controlled using a computer-programmable translation stage (Thorlabs). Following the sample is another linear polarizer, which is oriented perpendicular to the initial polarizers and acts as an analyzer. The two beams are then separated using a combination of beam splitter and band-pass filters at individual wavelengths. The detection is provided by two photodiodes (Thorlabs), followed by respective wide-bandwidth amplifiers (Melles-Griot). Phase-sensitive detection is provided by two lock-in amplifiers (Stanford Research Systems). These signals serve as inputs to a digital controller programmed in LabVIEW 8.5 (National Instruments). The controller is essentially a proportional-integral-derivative (PID) controller providing

real-time closed-loop feedback. The output of the PID controller is connected to the respective Faraday compensators via a driver circuit.

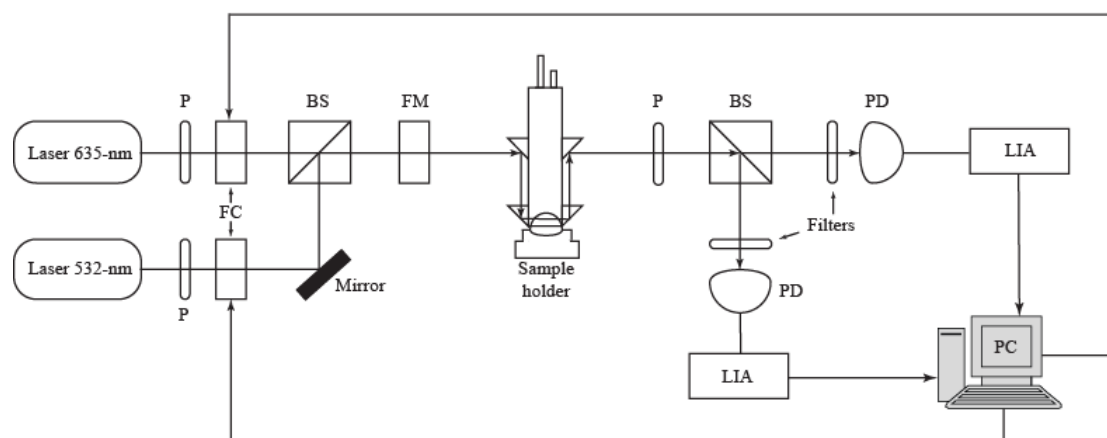


Figure 20. Experimental setup of the dual-wavelength optical polarimeter. Note that the sample holder can either be a plastic cuvette, the plastic ocular phantom or the artificial anterior chamber phantom for fixing isolated corneas. The two ports on the top of the eye coupling device are used to fill in the tube with PBS solution in order to accomplish index matching. P, polarizer; FC, Faraday compensator; BS, beam-splitter; FM, Faraday modulator; PD, photodetector; LIA, lock-in amplifiers.

The operation of this system is described by the following equation [20]:

$$I \propto \left(\varphi^2 + \frac{\theta_m^2}{2} \right) + 2\varphi\theta_m \sin(\omega_m t) - \frac{\theta_m}{2} \cos(2\omega_m t) \quad (3)$$

where I is the intensity of the detected signal, θ_m is the angular modulation depth provided by the modulating faraday rotator, ω_m is the modulation frequency, and φ is the rotation due to the optically active sample. It follows from Equation (3) that without an optically active sample and with the DC term removed, the detected signal consists only of the double frequency (2ω) term. When the optically active sample is introduced, the detected signal becomes an asymmetric sinusoid, which contains both the fundamental (ω) and the double frequency components.

In the case of a glucose sample with no birefringence, the φ term represents rotation only due to glucose and hence the glucose concentration can be measured directly by the feedback provided to close the system loop. However, in the case of a birefringent sample, the φ term includes both optical activity and rotation due to birefringence. This makes the extraction of change due to glucose in the presence of birefringence impossible by using a single wavelength approach, unless some type of birefringence compensation is utilized. To overcome this problem, our system utilizes two separate wavelengths in order to compensate for the effect of birefringence which is observed for both the wavelengths.

Control System

In past, a combination of simple proportional control and linear scanning for closed-loop polarimetry has been utilized [20, 91], whereby the output of the control system is the input multiplied by a user-defined calibration factor and then a small range of voltages were scanned to ultimately null the system. Although effective for a slower moving birefringence, the dynamic response of such a system would not be adequate for in vivo studies. Here we compare the performance of a closed-loop system with an open-loop system using dual wavelengths. In the case of the open-loop system, the total gain of the system is fixed and is dependent mainly on the system electronics. Also, due to the open-loop nature of this process, the output is not observable by the system and hence the system is incapable of rejecting any disturbances. For the closed-loop case, we have utilized a PID control mechanism to stabilize our feedback system and to provide optimal dynamic response. Although the use of proportional feedback control can reduce the error due to disturbances in the system, a constant input can still result in non-zero steady-state error. A common way of eliminating such error is to add a controller term proportional to the integral of the error. This virtually eliminates this error since the integral term is the sum of all past values of the error. In our current polarimetric system, the disturbance originates due to variation in birefringence of the sample. Inclusion of an integrator usually deteriorates the dynamic response of the system. This is overcome by addition of a differentiator to the control system which significantly improves the dynamic response. The PID gain parameters were optimized using Ziegler-Nichols tuning rules [92]. In this method, the conditions for adjusting the PID parameters are

based on estimating the amplitude and frequency of oscillations of the system at the point of marginal stability. In general, the controller settings according to Ziegler-Nichols rules provide acceptable closed-loop response for most systems.

Faraday Rotators

The Faraday rotators, used for both modulation and compensation, consist of 1-cm long Terbium-Gallium-Garnet (TGG) crystals (Deltronic Crystals, Inc.) inside electrical coils. TGG crystals were employed since it is one of the highest Verdet-constant magneto-optic materials commercially available and the optical losses involved therein are lower than that of other high Verdet-constant materials. The solenoid is made up of ~3500 turns of 30 gauge magnetic wire around a custom-machined bobbin made out of Delrin, a commonly available engineering thermoplastic. A low power audio amplifier is utilized to provide the modulation signal to the Faraday coil which is connected in serial to a 0.1 μF capacitor in order to achieve resonance at the modulation frequency of 1.09 kHz. For compensation, a simple operational amplifier driver circuit was used.

Eye Coupling Mechanism

An in-house built eye coupling device, shown in Figure 21, was used to couple light in and out of the anterior chamber of the eye phantom. The device consists of an inverted glass tube with four 1-cm reflecting prisms (Thorlabs, Newton, NJ) attached in a periscope configuration. The glass tube is filled with phosphate buffered saline (PBS) solution which allows for index-matched coupling through the mounted *ex vivo* corneas,

and resulted in a straight path through the anterior chamber while minimizing beam divergence and deflection [93]. The presence of PBS solution also kept the cornea hydrated and helped reduce epithelium degradation [68].

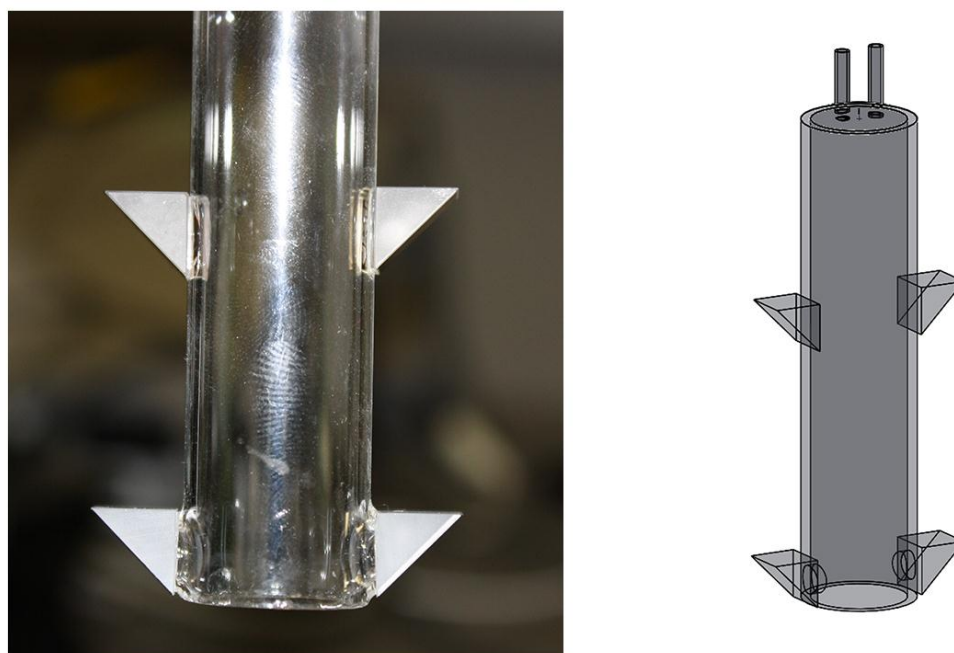


Figure 21. Photograph (left) and CAD model (right) of the eye coupling device. The glass test tube can be filled with PBS solution to allow for index-matched coupling through the isolated corneas clamped on the artificial anterior chamber phantom.

Plastic Eye Model

For in vitro operation, a custom-built ocular eye model (Ocular Instrument Inc., Bellevue, WA) was used to mimic the anterior chamber of the eye. As shown in Figure 22, the anterior chamber of the eye was retrofitted with 0.5 mm infusion tubes. This modification allowed changing the glucose concentration in the anterior chamber. The cornea is made out of Poly (methyl methacrylate) (PMMA) which has a refractive index of 1.489. The relative index mismatch between the refractive indices of PMMA and PBS ($n = 1.33$) did not allow for perfect index matched coupling using the above mentioned eye coupling device. Instead, the anterior chamber was immersed in a large glass cuvette (Starna Cells, Inc., Atascadero, CA) filled with PBS. The index mismatch resulted in a slight deviation of the beam leaving the anterior chamber relative to the input beam and, therefore, the detection side of the optical system had to be adjusted accordingly. Finally, the eye was mounted on a programmable translation stage to induce motion artifact.

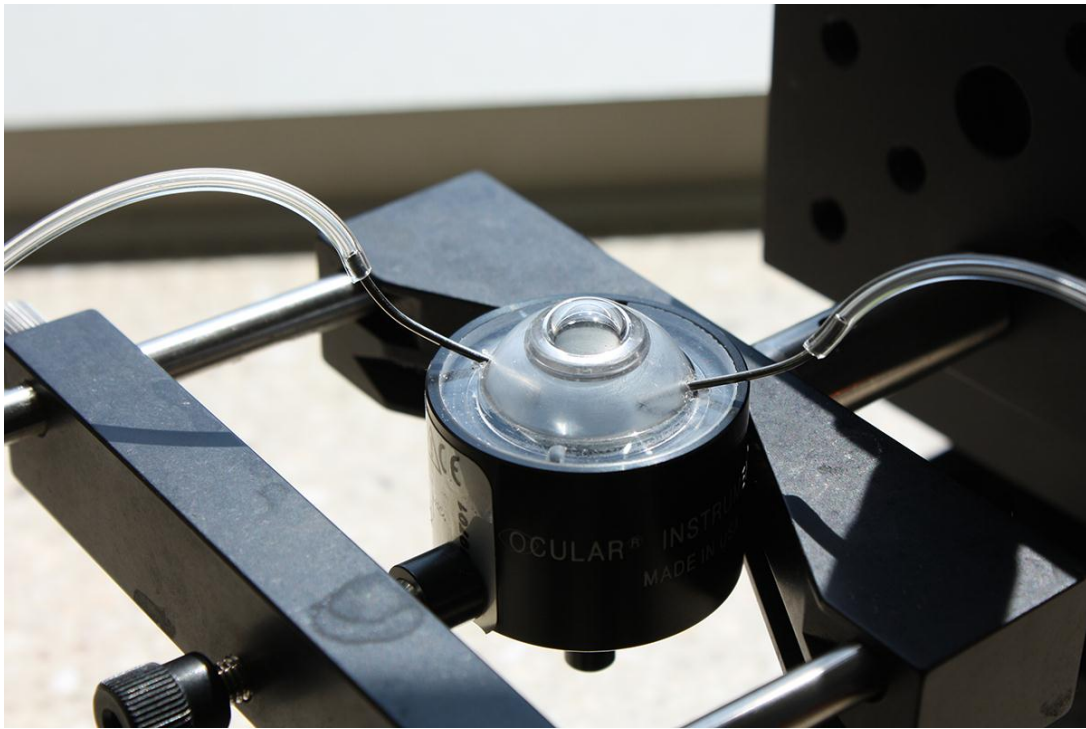


Figure 22. Photograph of the custom-built ocular model. Note that the chamber is fitted with two infusion tubes, which allows changing of glucose concentration in the anterior section.

Ex Vivo Mounted Corneas

Corneas ($n = 3$) were harvested from New Zealand White rabbits. All corneas were visually inspected, and were visibly transparent before, during and after the *ex vivo* measurements. Excised corneas with 2-3 mm of scleral rim were mounted on an artificial anterior chamber (Katena Products, Denville, NJ) as shown in Figure 23. The base of the chamber comes fitted with two ports to inflate the anterior chamber, which were used to change the glucose concentration in the anterior chamber of the eye. The hydrostatic pressure within the chamber was maintained at the intra ocular pressure level of 15 ± 0.1 mmHg. Similar to the plastic eye phantom, the mount to hold the artificial chamber was fitted on a translation stage to achieve motion artifact.



Figure 23. Photograph of an isolated cornea clamped on the artificial anterior chamber. Note that the clamping region is within the sclera which can minimize stress on cornea.

In Vivo Animal Studies

Three New Zealand White rabbits (Harlan, Indianapolis, IN) weighing 2.27 kg to 2.50 kg were used. The anesthesia regimen was formulated by mixing the 9 ml Ketamine (100mg/ml), 3 ml Acepromazine (10mg/ml) and 1.8 ml L. A. Rompun (100 mg/ml) in 7.2 ml of saline solution. The resultant cocktail was administered intramuscularly at the rate of 1 ml per 1.5 kg body weight. After anesthesia, the rabbits were placed on an adjustable platform underneath the eye coupling device, as shown in Figure 24-25. The coupling device was then lowered slowly over the rabbit's eye until contact was made. The inverted glass tube was then filled with saline solution to accomplish index matching at the corneal interface. Placing a rubber o-ring coated with an eye hydration ointment helped seal the gap and minimized fluid leakage.

Initially, complete blood analyses were performed to measure the blood glucose levels during anesthesia. This is important since the xylazine in anesthesia is known to have a strong hyperglycemic effect due to its blocking of the pancreatic insulin release through stimulation of parasympathetic receptors [94, 95]. Consequently, the content of glucose in the aqueous humor is increased considerably. While, such behavior can be regarded as the inducing factor for cataractous changes seen in animals with a low tolerance to high glucose levels in aqueous humor, the effect is desirable for in our animal study. The anesthesia regimen serves a dual purpose of working as a bolus injection of glucose, otherwise difficult to induce in rabbits without diabetes. During the course of the experiment, 1-ml blood samples were withdrawn every ~10 minutes and were analyzed using both a hand-held blood glucose meter (Accu-Chek Aviva system)

and the YSI 2300 glucose analyzer. These measurements provided useful information related to trends in the blood glucose levels which potentially correlate to aqueous humor glucose levels.



Figure 24. Photograph of the eye coupling device. Note that the double periscope configuration allows for a direct light path through the eye which, otherwise, would be blocked by rabbit's facial features.

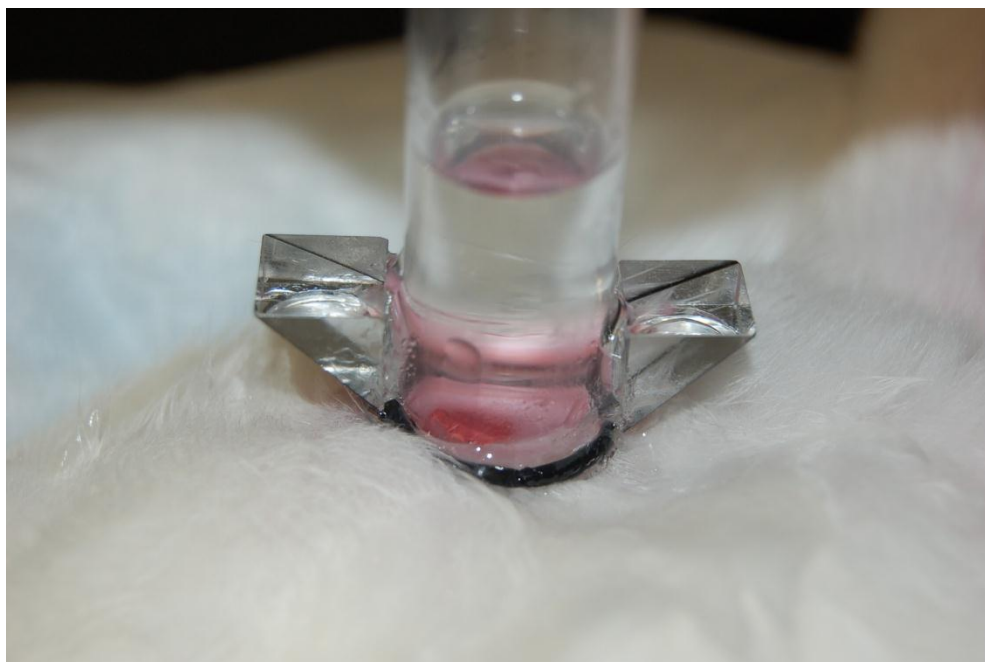


Figure 25. Photograph of the eye coupling device placed on the rabbit eye. Note that the test tube is filled with saline solution to allow for index matching.

Results and Discussion

In Vitro Experiments using Glucose Samples in a Cuvette

For open-loop operation, the system was first calibrated without motion using simple linear regression. This provides the conversion factors required to convert the measured signal at the lock-in amplifier to the respective glucose concentrations. This was followed by validation experiments, repeated four times on a moving birefringent sample cuvette. The glucose concentration was varied in the physiologic range of 0 to 600 mg/dl in 50-mg/dl steps. Simple linear regression was applied to the data for individual wavelengths. Figures 26 and 27 show estimated glucose concentration as a function of the actual glucose concentration. It is evident that a single wavelength open-loop system at either wavelength is incapable of estimating glucose concentration in a test cell with time-variant birefringence. For instance, the mean error in prediction of glucose was calculated to be 186.9 mg/dl and 185.6 mg/dl, with R^2 -values of 0.149 and 0.166, respectively. This calculated value of error in glucose estimation is an average of errors in glucose estimation for four individual sets. It does not take into account the effect of using a single calibration model to validate separate data sets, the effect of which can be seen as the extent of error bars in Figures 26 and 27 which are an order of magnitude larger than the mean error in glucose estimation. This variation between data sets and thus the lack of repeatability is a result of the open-loop nature of the system, which makes it unfeasible to use a single calibration model for validation. Hence these error bars signify both the error due to time variant birefringence and due to the lack of repeatability from other noise disturbances. To see the effect of utilizing dual

wavelengths, the combined dual wavelength data was used in a multiple-linear regression analysis. The mean error in prediction of glucose was calculated to be slightly less at 181.8 mg/dl with R^2 -value of 0.516. As shown in Figure 28, the magnitude of error bars is also noticeably less but the open-loop system is still incapable of estimating glucose concentrations in the physiologic range.

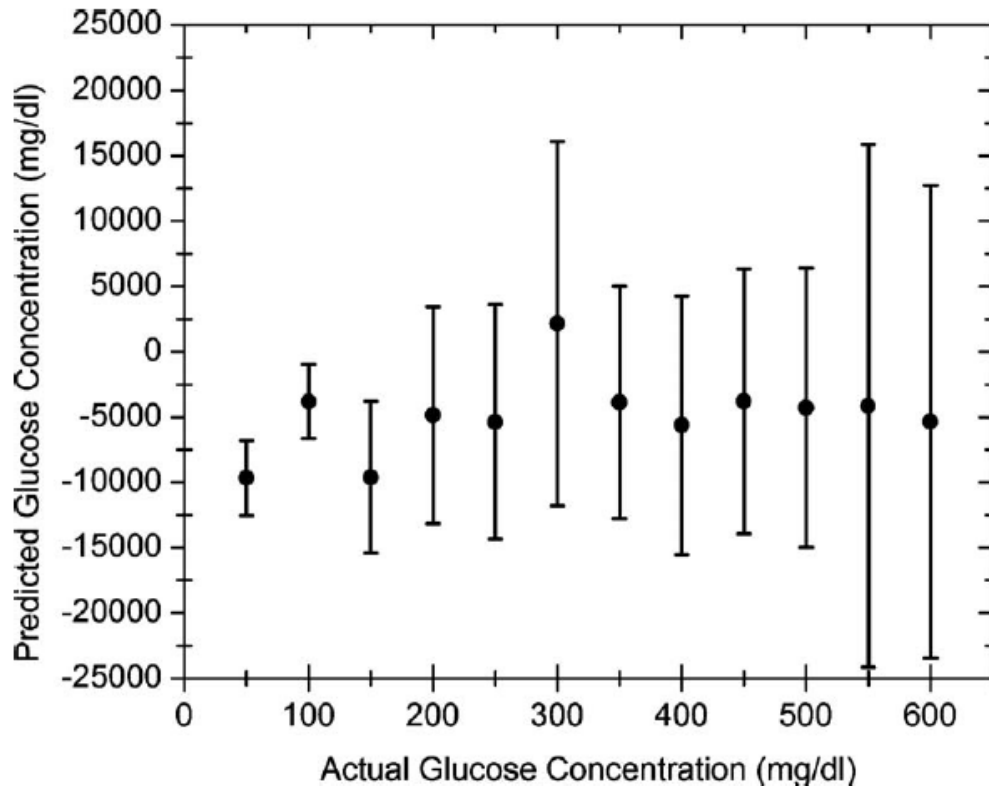


Figure 26. Mean estimated glucose concentration as a function of actual glucose concentration for an open-loop single wavelength model using the 635 nm wavelength. Error bars represent variation between four separate experiments and are quite high as anticipated for this system in the presence of variable birefringence and other noise disturbances not compensated in an open-loop system.

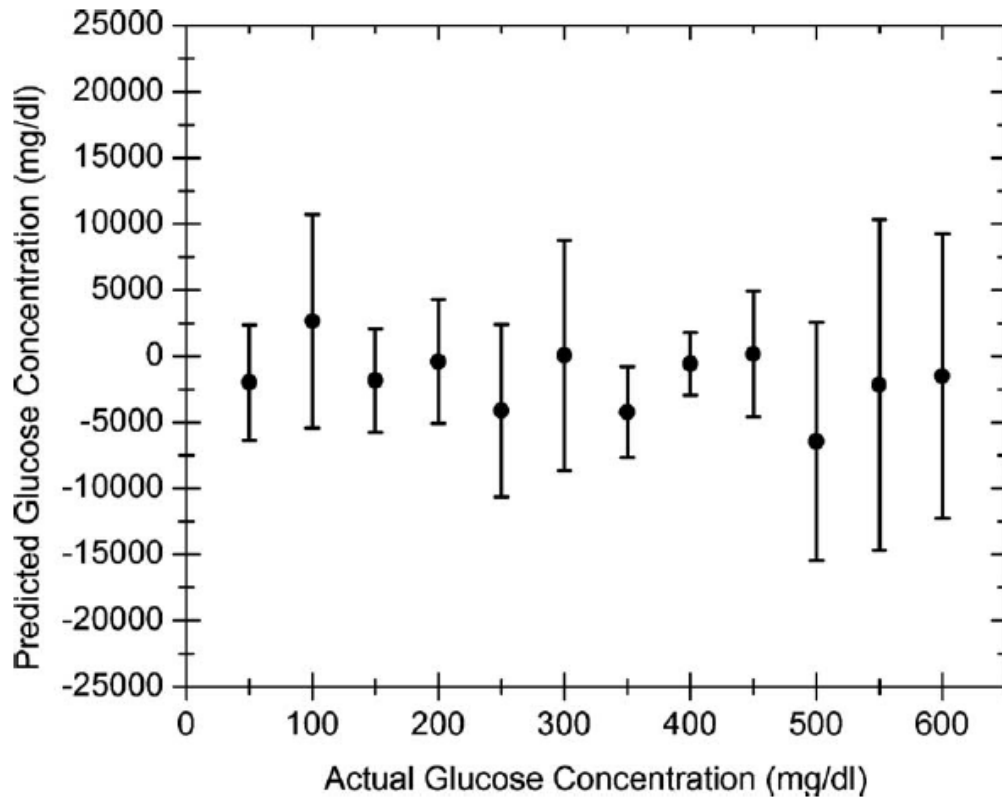


Figure 27. Mean estimated glucose concentration as a function of actual glucose concentration for an open-loop single wavelength model using the 830 nm wavelength. Error bars represent variation between four separate experiments and are quite high as anticipated for this system in the presence of variable birefringence and other noise disturbances not compensated in an open-loop system.

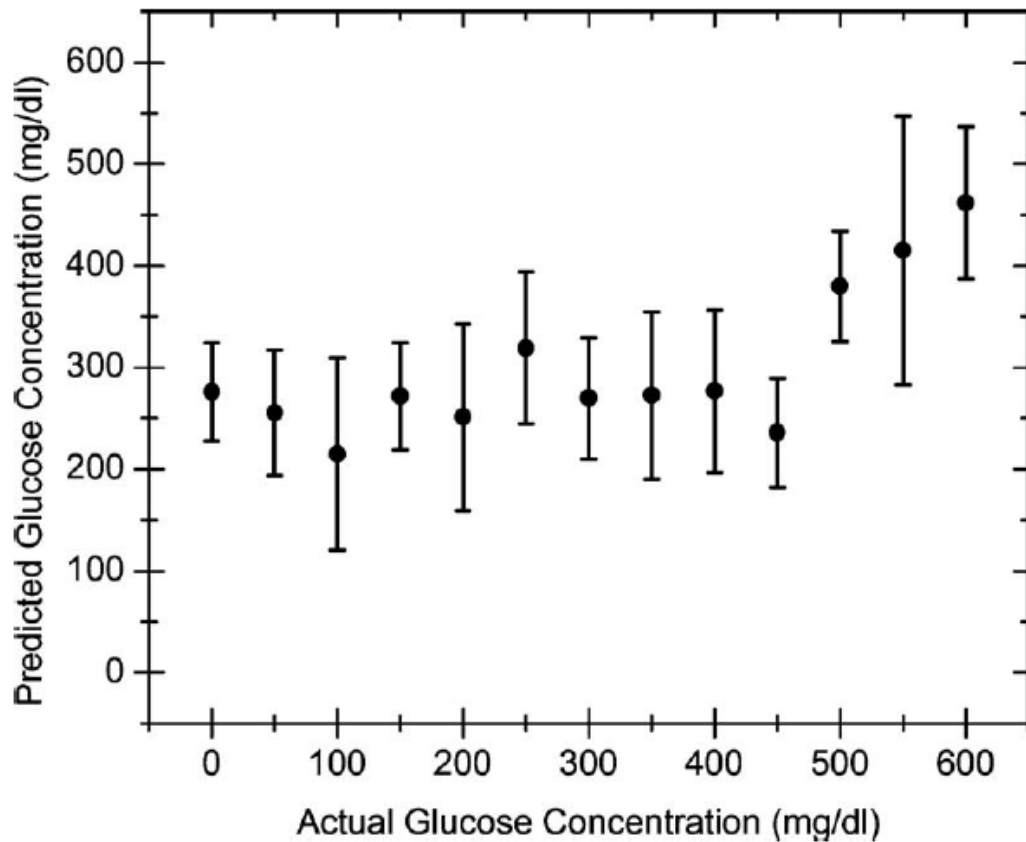


Figure 28. Mean predicted glucose concentrations for the real-time open-loop dual wavelength system using a multi-regression model. Error bars represent variation between four separate runs of experiments. Note that the open-loop dual wavelength system significantly reduced the magnitude of the error bars compared to single wavelength system but they are still much too high for physiologic monitoring due to other noise disturbances not compensated by the open loop system.

The system was then calibrated for closed-loop operation followed by validation experiments, again repeated four times. The feedback loops for both wavelengths were closed in near real-time simultaneously using two separate PID controllers programmed in LabVIEW. The data acquisition time was set to be ~ 500 ms which was just over the time taken by the control mechanism to stabilize the system. Figures 29-30 show the predicted glucose concentration as a function of actual glucose concentration for the closed-loop case. It is evident that the variation in between different data sets is reduced since the scale of error bars is an order of magnitude less when compared to open-loop single-wavelength system (Figures 26 and 27). However, this is not enough to accurately determine sample glucose concentration. The mean error in estimation of glucose was calculated to be 164.6 mg/dl and 131.6 mg/dl, with mean R^2 -values of 0.566 and 0.355 for 635 nm and 830 nm wavelengths, respectively. This result demonstrates the problem of how the change in the birefringence of the sample cloaks the optical rotation due to glucose. To compensate for the effect of this birefringence, the single wavelength data for both the wavelengths was used in a MLR analysis. As shown in Figure 31, this analysis considerably increased the overall linearity of the collected data - mean R^2 -value of 0.996 - and reduced the mean error in estimation of glucose to 12.8 mg/dl. The application of multiple-linear regression is analogous to scaled subtraction. The general idea is to use this regression analysis to predict the contribution of birefringence to the total rotation of state of polarization. The data points for both wavelengths are used to calculate optimal weights for respective data sets. Once these coefficients are determined, the sample noise can be removed by subtracting the scaled data sets. The

overall result is reduction in the effect of time-varying birefringence due to motion artifact which manifests as sample noise for both the wavelengths.

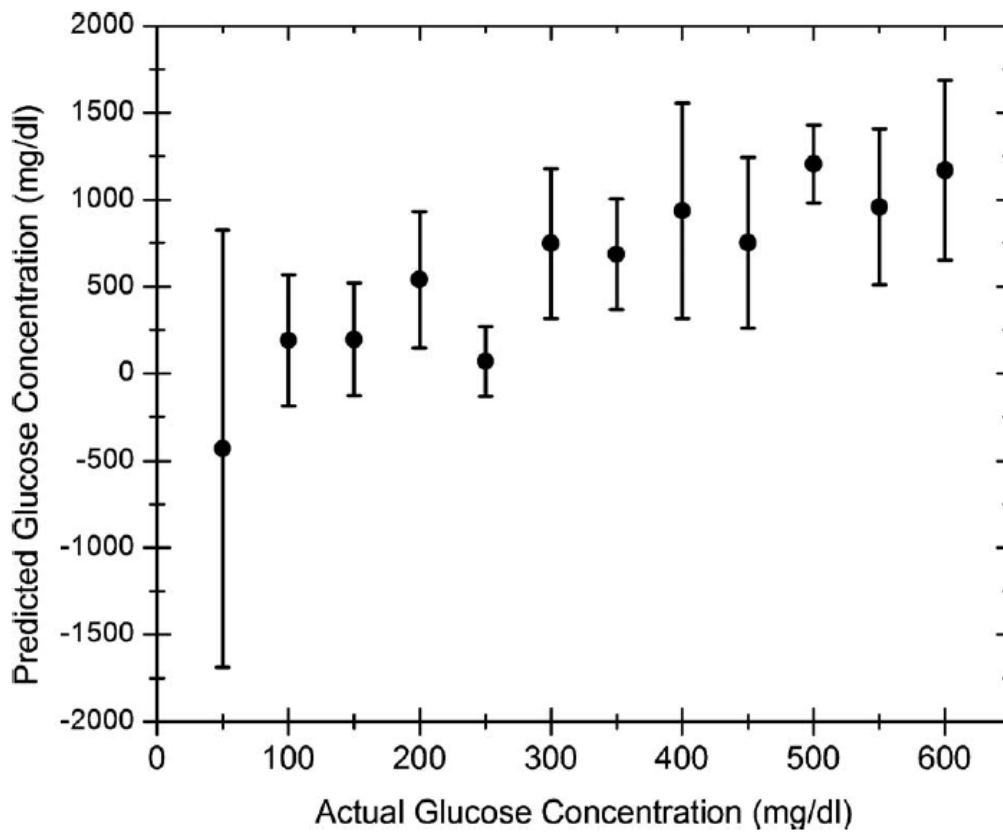


Figure 29. Mean estimated glucose concentration as a function of actual glucose concentration for a closed-loop single wavelength model using the 635 nm wavelength. Error bars represent variation between four separate experiments. Note that the closed-loop single wavelength system cannot accommodate for the time-varying birefringence.

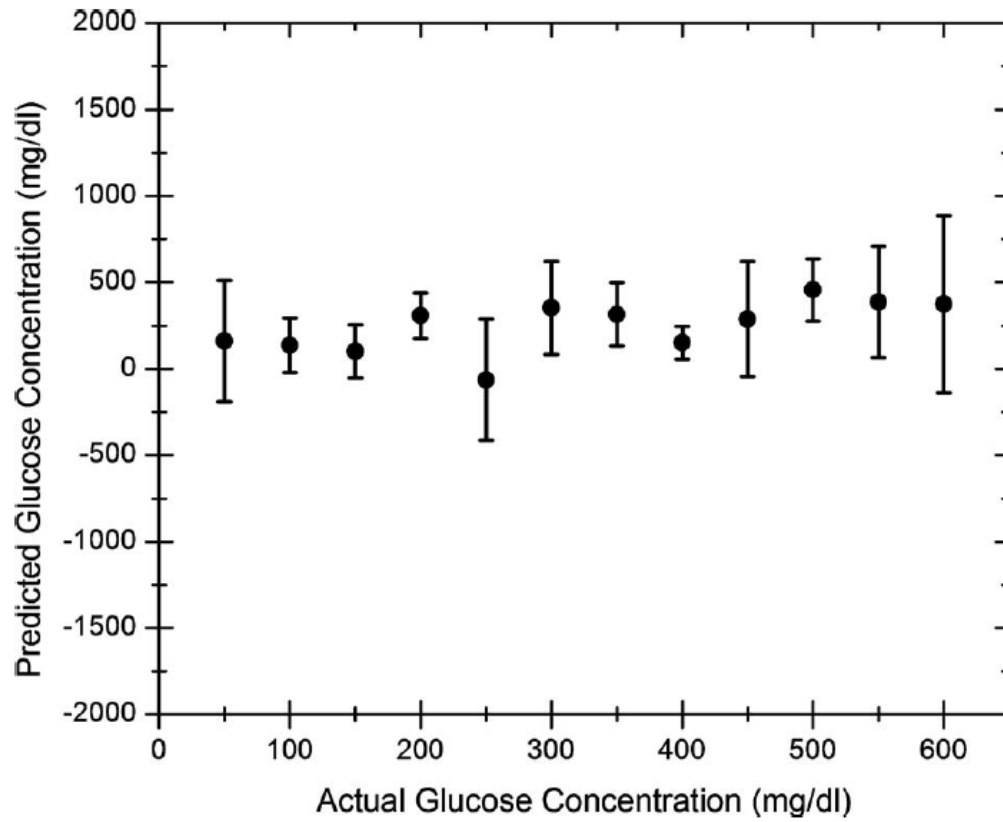


Figure 30. Mean estimated glucose concentration as a function of actual glucose concentration for a closed-loop single wavelength model using the 830 nm wavelength. Error bars represent variation between four separate experiments. Note that the closed-loop single wavelength system cannot accommodate for the time-varying birefringence.

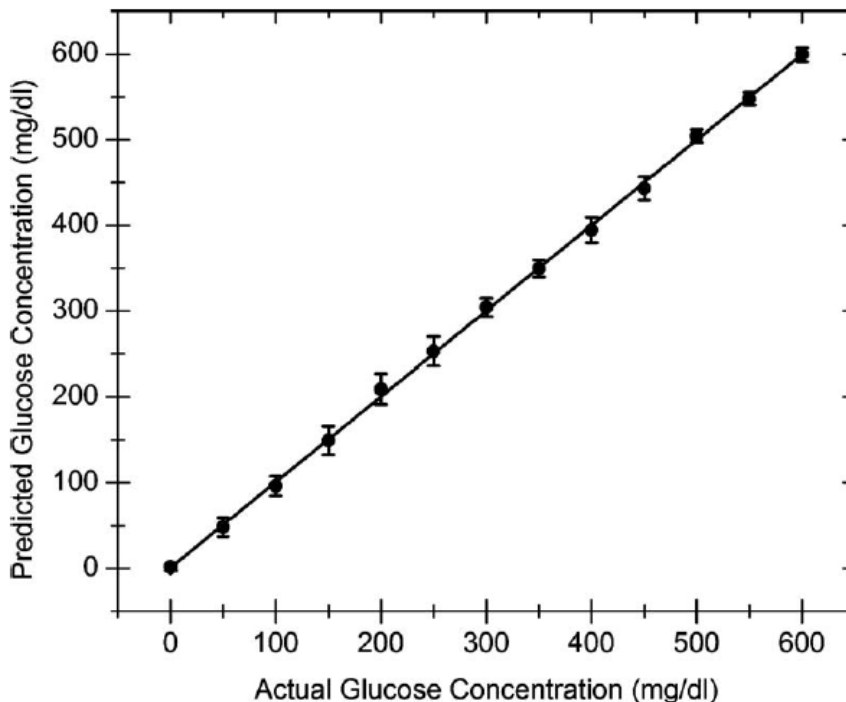


Figure 31. Mean predicted glucose concentrations for the real-time closed-loop dual wavelength system using a multi-regression model. Error bars represent variation between four separate runs of experiments. Note that the dual wavelength real-time PID closed-loop system can be used to accommodate time-varying birefringence.

These results demonstrate the advantages of using a closed-loop system over an open-loop system, and the dual-wavelength system compared to the single-wavelength system for the case of time varying birefringence. By the way of theoretical background, closed-loop systems are much more efficient in rejecting disturbances [92]. They are also less sensitive to random fluctuations in operating conditions which makes them less susceptible to noise. Previously reported optical polarimetric techniques have utilized feedback based on scan-based algorithms [24, 30], which have intrinsically slow

dynamic response for zero steady-state error. Our proposed approach utilizes dual wavelength, near real-time, feedback using PID control. The use of real-time feedback is important since the ultimate application of this technique is to reduce the effect of time-variant corneal birefringence in the eye.

In Vitro Experiments using Plastic Ocular Phantom

The results of the dual wavelength polarimetric system for determining glucose concentration inside the anterior chamber of the plastic eye phantom are presented in Figures 32–33. The experiment was also repeated four times across the physiologic glucose concentration range. Figure 32(a) and 32(b) show the single-wavelength polarimetric measurements for 635-nm and 532-nm wavelengths, respectively. As anticipated, these results indicate that a linear model based on a single wavelength is unable to predict glucose concentration in presence of motion artifact. As mentioned earlier, such a system is unable to differentiate between the rotation due to optical activity of glucose and due to the time varying birefringence. The mean standard error of prediction of glucose concentration is 113.5 mg/dL and 136.5 mg/dL for the wavelengths of 635 nm and 532 nm, respectively. However, when the measurements from individual single wavelengths are treated with multiple linear regression (MLR) analysis, the effect of birefringence is significantly reduced as shown in Fig. 33. The dual wavelength system response is much more linear in comparison to either individual wavelength response and the mean standard error of prediction is reduced by an order of magnitude to 14.5 mg/dL with a correlation coefficient of 0.998.

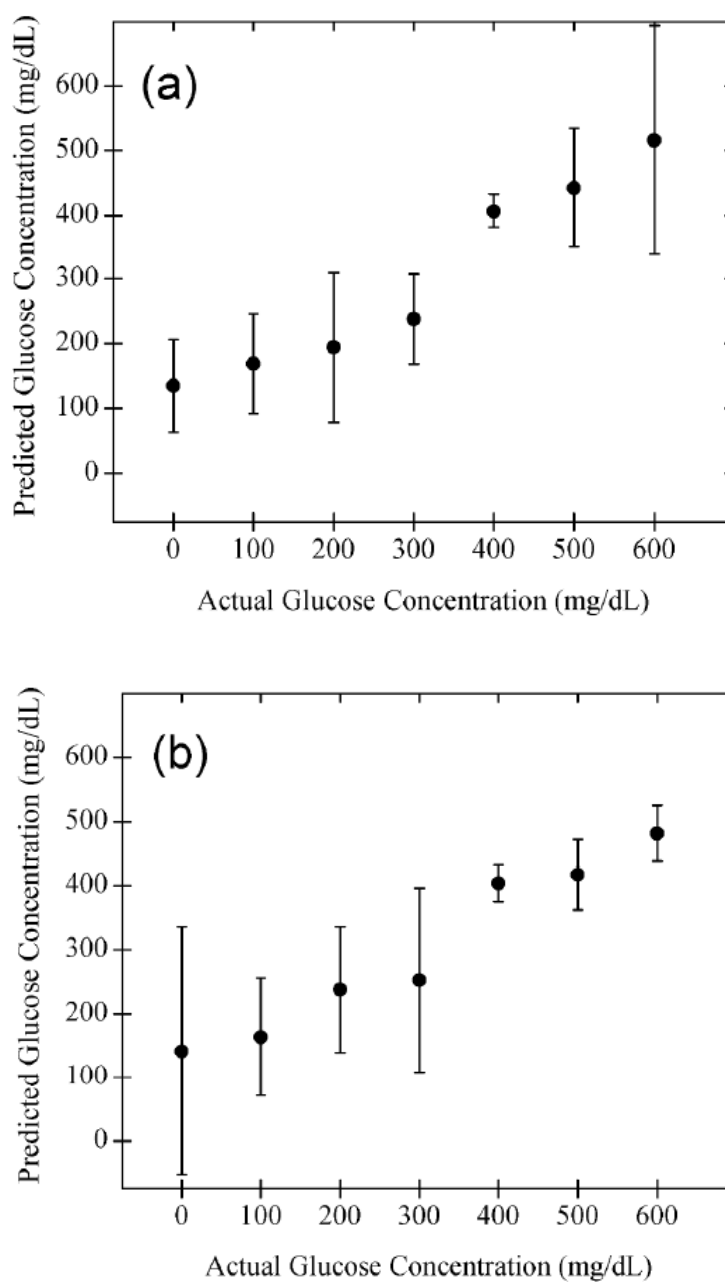


Figure 32. Mean estimated glucose concentration as a function of actual glucose concentration for the *in vitro* single wavelength model using (a) 635-nm, and (b) 532-nm wavelengths. Note that the error bars represent the variation between four separate experiments and are large, showing the inability of a single wavelength model to predict glucose concentration.

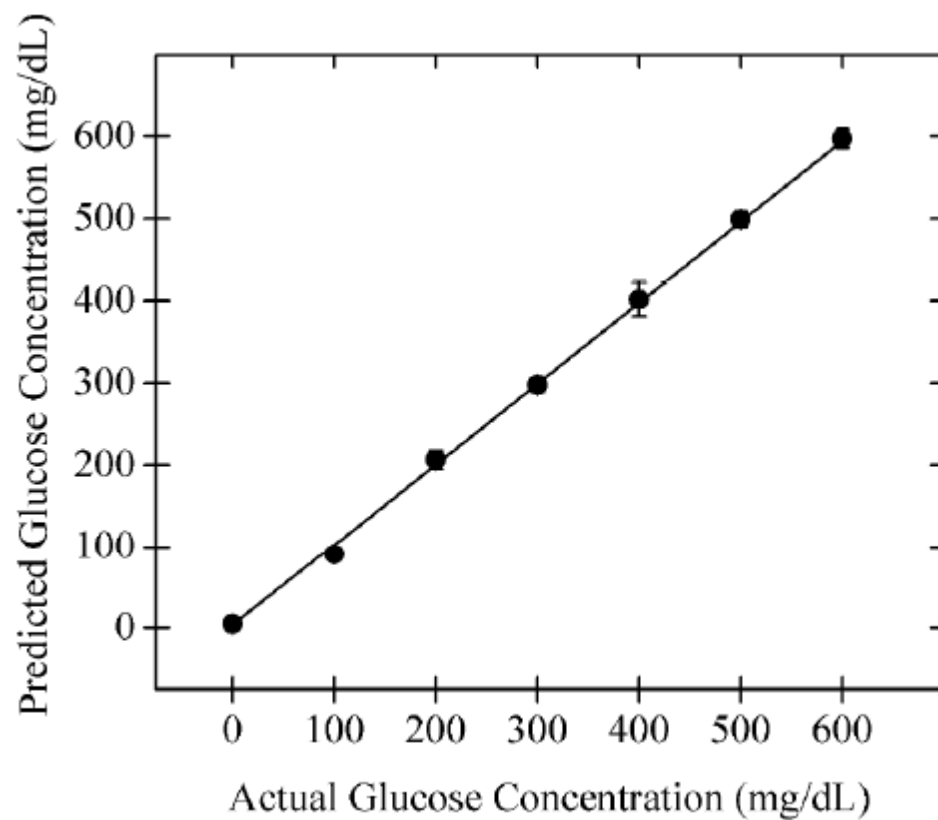


Figure 33. Mean estimated glucose concentration as a function of actual glucose concentration for the *in vitro* dual wavelength model. The error bars represent the variation between four separate experiments and are significantly reduced relative to the single wavelength models.

Ex Vivo Experiments using Isolated Corneas

While the application of dual wavelength polarimetry to *in vitro* glucose sensing in the plastic eye model serves to demonstrate how this method may be applied *in vivo*, physiologic sample noise conditions due to actual corneal birefringence as well as the refractive index difference between cornea (1.376) and the polymer (1.489) are somewhat different. Therefore, we extended the application of our approach to isolated corneas mounted on an artificial eye anterior chamber. Since our eye coupling mechanism allows the light to travel straight through the anterior chamber, without interacting with any ocular tissues other than the cornea, the isolated corneas more closely represent physiologic conditions. Although, clamping corneas at the scleral rim can create artificial boundary conditions which can potentially affect corneal birefringence, the clamping geometry of the artificial chamber in our phantom minimized the stress on the sclera [96].

The results of our polarimetric approach for determining glucose concentration inside the corneas clamped on an artificial anterior chamber are presented in Figures 34–35. Similar to the *in vitro* results, a single wavelength system using either wavelength is unable to predict the glucose concentration *ex vivo* with required precision. The mean standard error of estimation is calculated to be 125.4 mg/dL and 151.1 mg/dL for the individual wavelengths of 635 nm and 532 nm, respectively. However, when the information from both the wavelengths is combined and analyzed using MLR, the error in estimation is reduced significantly to a mean value of 22.4 mg/dL and appeared much more linear with a correlation coefficient of 0.996. This further demonstrates the

potential of the dual-wavelength approach to compensate for the time varying corneal birefringence.

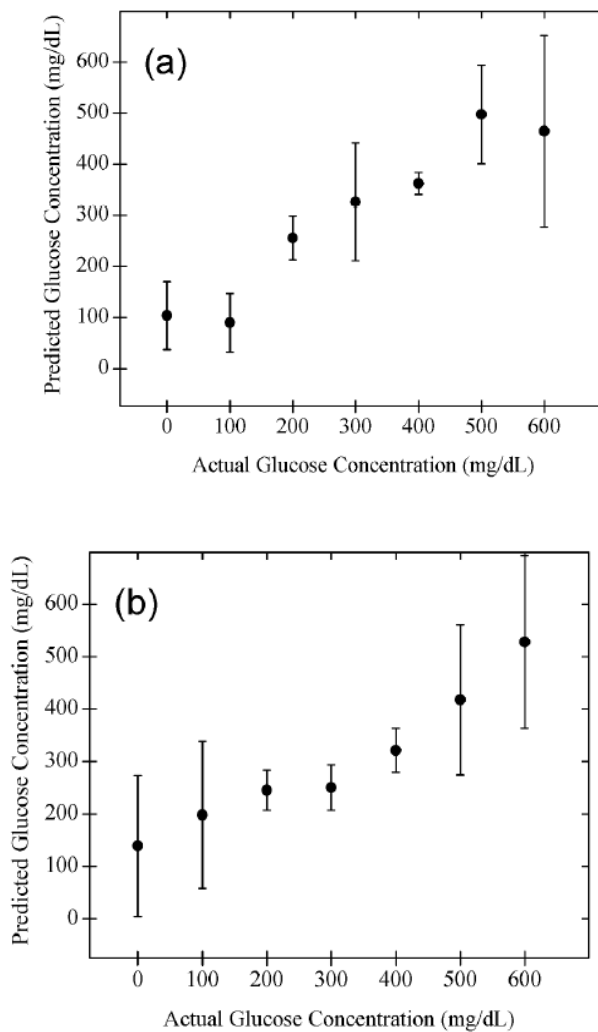


Figure 34. Mean estimated glucose concentration as a function of actual glucose concentration for the *ex vivo* single wavelength model using (a) 635-nm, and (b) 532-nm wavelengths. Note that the error bars represent the variation between three separate experiments and are large, showing the inability of a single wavelength model to predict glucose concentration.

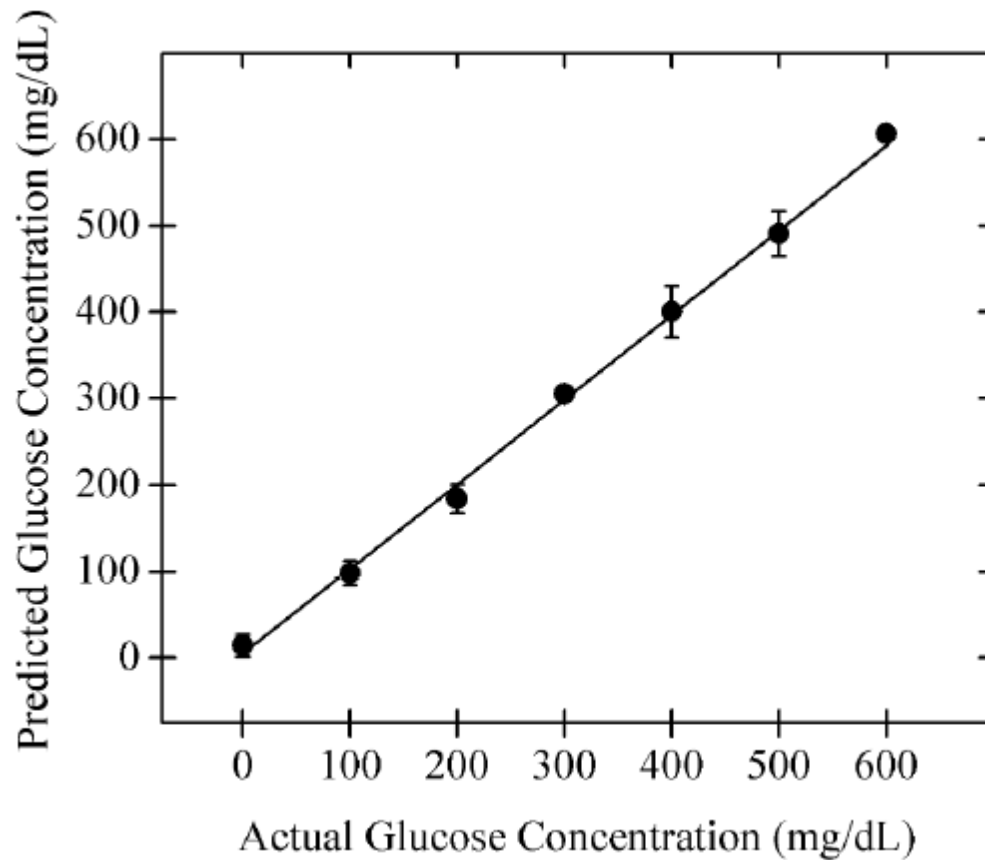


Figure 35. Mean estimated glucose concentration as a function of actual glucose concentration for the *ex vivo* dual wavelength model. The error bars represent the variation between three separate experiments and are significantly reduced relative to the single wavelength models.

It was noted that the noise in measurement signal was slightly more pronounced in the case of *ex vivo* cornea experiments in comparison to *in vitro* plastic phantom experiments, and is evident by the sensitivity of the system in the respective experiments. We believe that one of the major factors contributing to this relatively reduced accuracy is the corneal tissue compliance. Although, the clamping of the cornea

approximates the *in vivo* environment, changing the glucose concentration in the artificial anterior chamber results in a pressure cycle. This behavior has been previously studied in detail by Boyce et al. [97]. In their constrained inflation experiments, it was observed that the viscoelastic behavior of cornea generated hysteresis in the pressure-deformation response at the apical region. Such behavior can physically move the region on cornea being probed by the laser beam, during and in between measurements, resulting in a long-term drift in the polarimetric signal. We quantified this sample noise by determining the variation within and across signal measurements. As mentioned above, each measurement is based on a ten-point running average. The standard deviation within these ten points in a single measurement, in terms of glucose concentration, was found out to be similar (~ 6 mg/dL) for both *in vitro* plastic phantom and *ex vivo* cornea phantom measurements. In contrast, the standard deviation of ten disparate measurements taken at one-minute time intervals was relatively higher for *ex vivo* isolated cornea measurements (~ 65 mg/dL) when compared to that for *in vitro* plastic phantom measurements (~ 17 mg/dL). This corneal hysteresis type of response in the *ex vivo* cornea phantom experiments represents an artificial added noise source and the biomechanical response *in vivo* will clearly be much less pronounced since the intraocular pressure variation is controlled physiologically and is limited to a much smaller range in the normal eyes.

In Vivo Experiments in Rabbits

In order to gain an understanding of the hyperglycemic effect of xylazine, blood glucose measurements were done every five to ten minutes. Such a response for three different rabbits is shown in Figure 36. As can be seen, while the absolute values somewhat differ, all the rabbits exhibit the same general trend in blood glucose levels after the administration of anesthesia. The glucose levels tend to rise to over twice the initial levels and plateau around 55 – 60 minutes. These observations serve as a reference for polarimetric glucose measurements.

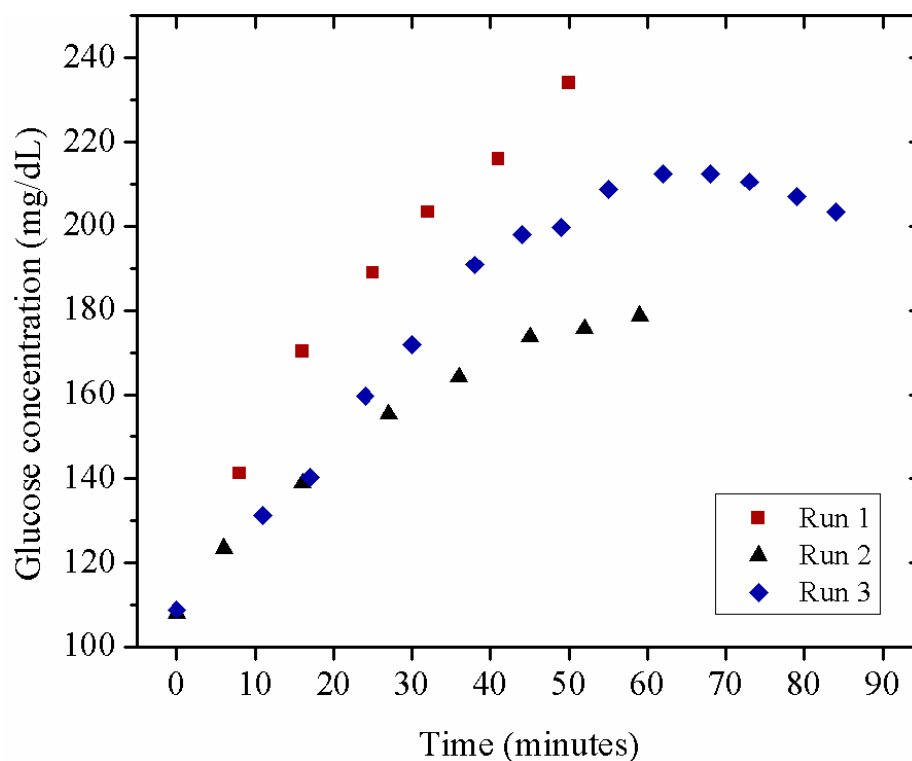


Figure 36. Blood glucose response in NZW rabbits after administration of anesthesia

The first run of polarimetric studies was performed to verify the operation of the eye coupling mechanism, and to test whether the light can be successfully coupled and transmitted through the anterior chamber of eye. In all the experiments to date, the coupling device has performed remarkably well in terms of coupling light through the anterior chamber of the eye. The beams at two different wavelengths follow an overlapping path throughout the device and the eye, and the output beams stay coincident at the detector input.

In order to ascertain the source of motion artifact in the detected signal, a portion of the feedback signal as a function of time was decomposed into its constituent frequencies using fast Fourier transform (FFT). Ideally, such a treatment should produce a DC value only, since the lock-in amplifier outputs a DC value proportional to the amplitude of the signal of interest. The frequency domain signal for both the wavelengths is shown in Figures 37 and 38 for two separate runs. In both the instances, the largest peak other than at DC occurs near 1.0 – 1.1 Hz range, and correlates well in between both the wavelengths. The variation in signal at this frequency is believed to be due to the motion artifact caused by the breathing cycle. The frequency of respiration i.e. breaths per minute in a NZW rabbit anesthetized using the ketamine/xylazine/acepromazine anesthesia can vary between 40 to 90 breaths per minute, and somewhat varies as a function of time since administration of anesthesia [98]. The peak near 0 Hz is due to the average value of time series signal. Other possible sources of motion artifact, including the cardiac cycle which occurs at 3-4 Hz, noticed previously [22] were not observed in this analysis.

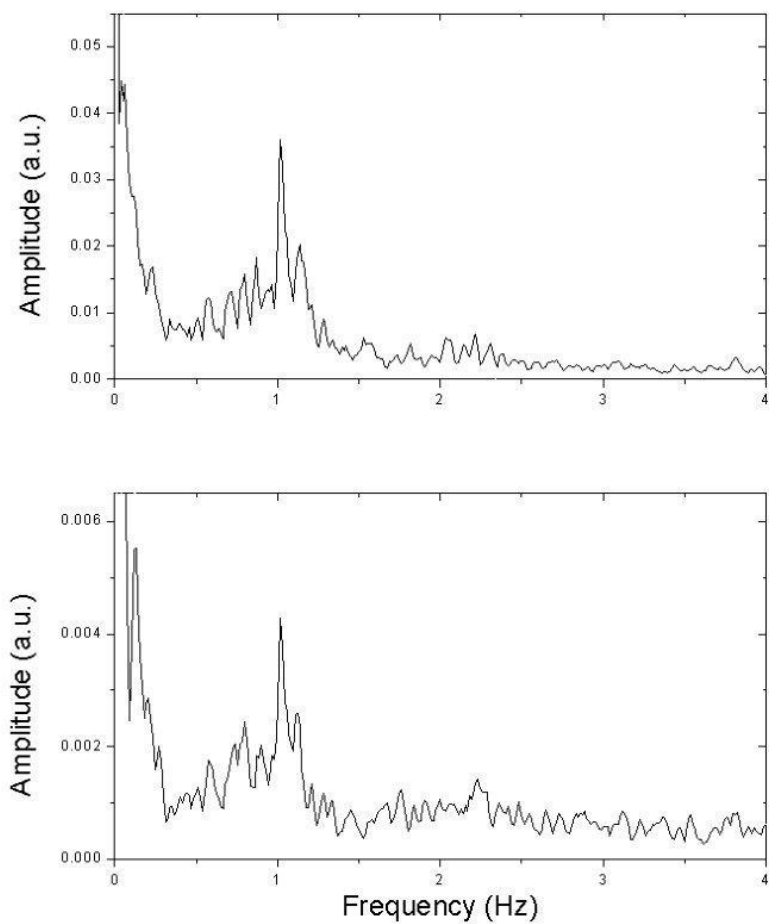


Figure 37. Spectral analysis of the time-based polarimetric feedback signal – Run 1; top: 635-nm feedback, bottom: 532-nm feedback.

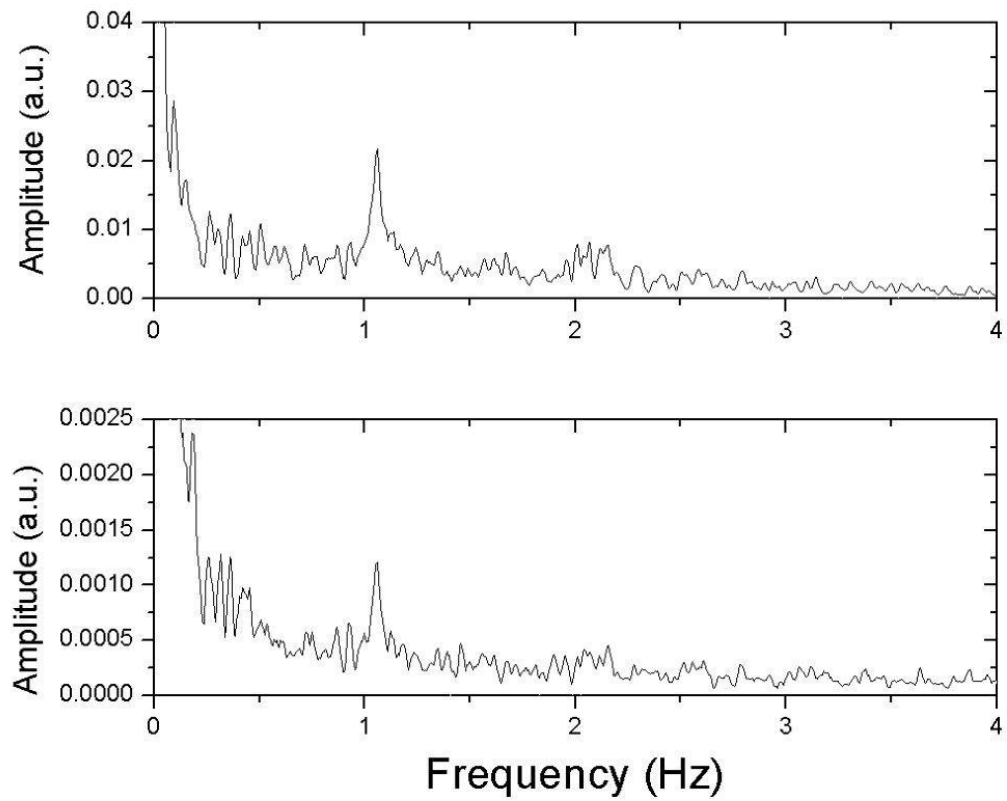


Figure 38. Spectral analysis of the time-based polarimetric feedback signal – Run 2; top: 635-nm feedback, bottom: 532-nm feedback.

Polarimetric glucose measurements were then performed *in vivo* using the dual-wavelength system. The single wavelength measurements are shown in Figure 39 and Figure 40 for the two individual wavelengths. The standard error in prediction of glucose concentration was calculated to 10 mg/dL and 7 mg/dL for the 635-nm and 532-nm single wavelength models, respectively. While these calculated error values are better than that of *in vitro* and *ex vivo* results, it should be noted that this estimation is over a much smaller glucose level change, which is approximately 33 mg/dL across the four data points. A percentage error is, therefore, a better indicator of the system sensitivity. The error values calculated above translate to ~30% and ~20% error for the 635-nm and 532-nm single wavelength models, respectively. Now, when the data from individual wavelengths is treated with MLR, the overall error is reduced to 6% (~2 mg/dL), as shown in Figure 41, demonstrating the potential of our approach to account for the time varying corneal birefringence due to eye motion artifact. Additional studies similar to the previous were performed with error in glucose estimation varying from 5% to 12%.

Although, the calculated errors seem quite low in terms of physiological glucose levels, a complete characterization of this technique would require varying blood glucose levels over a much larger range. At any rate, this investigation of optical polarimetry for glucose sensing shows considerable promise, and future work towards more robust eye coupling mechanism and sophisticated control systems can potentially improve the current design towards the ultimate development of a noninvasive glucose sensor.

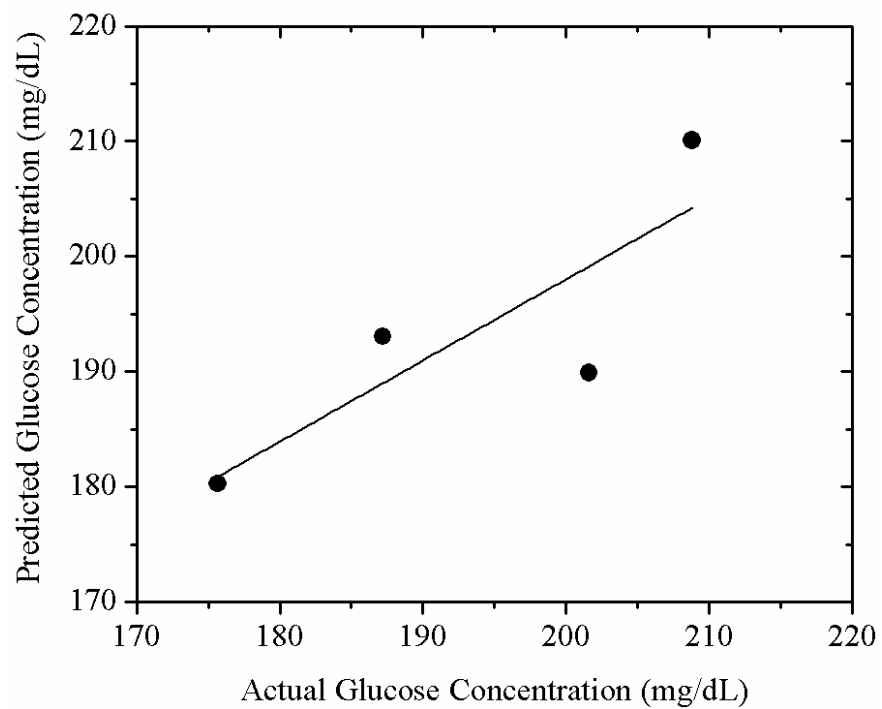


Figure 39. Predicted glucose concentration as a function of actual glucose concentration for the single wavelength model using the 635-nm wavelength.

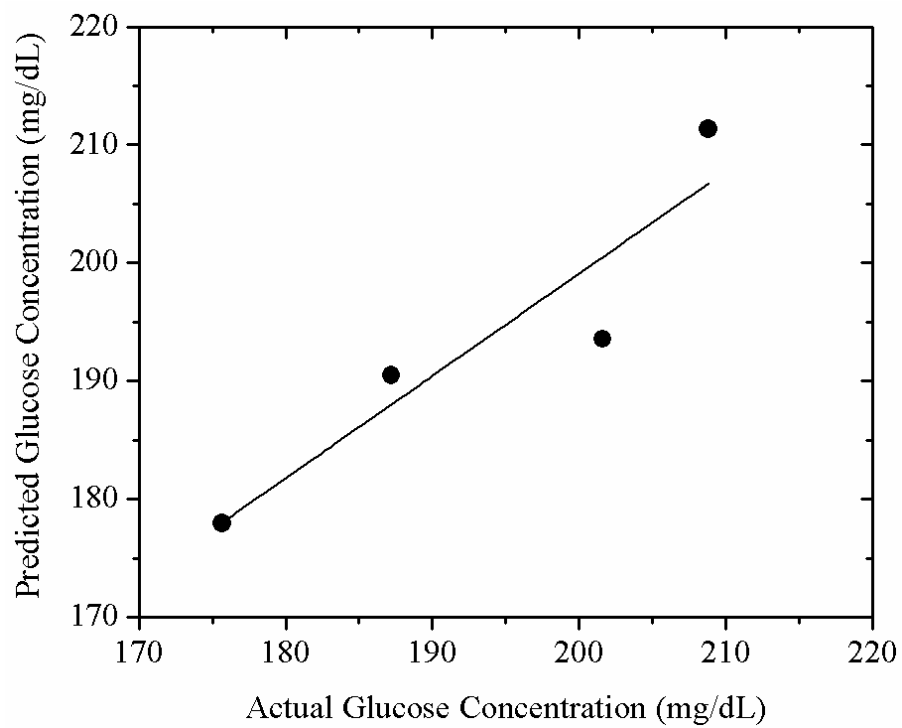


Figure 40. Predicted glucose concentration as a function of actual glucose concentration for the single wavelength model using the 532-nm wavelength.

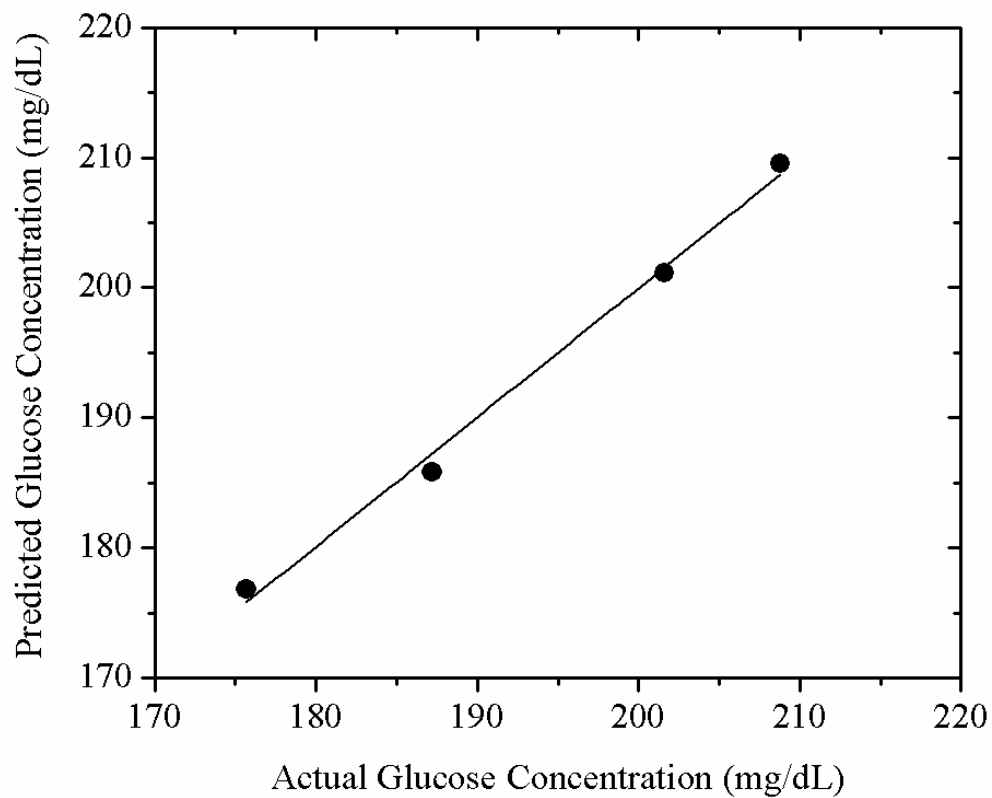


Figure 41. Predicted glucose concentration as a function of actual glucose concentration for the dual wavelength model. Note that the overall error in estimation of glucose is now reduced to 6% in comparison to 30% and 20% for 635-nm and 532-nm single wavelength models, respectively.

CHAPTER V

CONCLUSIONS AND FUTURE WORK

In summary, the goal of this research was to design and develop a noninvasive optical polarimetry technique to ultimately measure the glucose concentration in the anterior chamber of the eye as a means to ascertain blood glucose concentration.

The first part of this study was focused towards understanding and characterization of the corneal birefringence properties in the eye under both matched and unmatched refractive index conditions. The change in the light propagation and state of polarization of transmitted light were both modeled and experimentally measured. The corneal birefringence was shown to vary significantly as a function of both position and angle of incidence, but regions of relatively minimal net change were also observed. It was demonstrated that change in the polarization vector due to corneal birefringence is at least an order of magnitude larger than that due to the change in optical path length and glucose concentration. Experimental observations ascertain the validity of our theoretical framework towards modeling of peripheral corneal birefringence and, although the absolute values did not exactly match the model, the relative values were consistent between the experiments and model. Both the modeling and experiments showed the potential of using a dual-wavelength polarimetric approach towards measuring the aqueous humor glucose concentration as means to minimize the corneal birefringence noise and thus quantify blood glucose concentration. Overall, the knowledge gained from these experiments and modeling can be useful in understanding changes in

polarized light as it traverses an eye and will provide a framework for building an index-unmatched coupling system toward the ultimate development of an optical polarimeter for noninvasive *in vivo* glucose sensing.

The latter part of the dissertation focuses on design and development of a real-time optical polarimetric approach for glucose sensing utilizing two wavelengths. The use of second wavelength along with real-time feedback enabled the reduction of the effect of time-variant birefringence. This significantly enhanced the sensitivity of the system in the presence of motion artifact thereby reducing the error in glucose estimation by an order of a magnitude compared to a single wavelength model and compared to the open-loop dual wavelength model. The application of the system was then extended to probe glucose in a realistic plastic eye model and *ex vivo* using New Zealand White rabbits' corneas mounted on a pressurized artificial anterior chamber. The results demonstrate that the dual wavelength optical polarimetric approach can accurately determine the glucose concentration in the presence of time varying corneal birefringence due to motion artifact in the eye. Finally, the animal studies performed on the NZW rabbits indicate that the system has the potential for *in vivo* glucose sensing.

Future work should focus on creating higher speed feedback algorithms for *in vivo* studies in order to accommodate for potential saccadic eye movements which occur at a rate that is an order of magnitude faster than the motion artifact due to the respiratory and the cardiac cycles. The speed of the system can also be potentially enhanced by using faster modulation schemes. The current modulator design limits the modulation frequency to a few kHz. Improved modulator design which can tolerate higher

modulation frequencies may allow for faster demodulation mechanisms, thereby, decreasing the time taken by the control system to reach stability.

REFERENCES

1. American Diabetes Association, "Diabetes statistics: total prevalence of diabetes," <http://www.diabetes.org/diabetes-basics/diabetes-statistics>, accessed on Aug. 2, 2011.
2. Centers for Disease Control and Prevention, "National Diabetes Fact Sheet, 2011," http://www.cdc.gov/diabetes/pubs/pdf/ndfs_2011.pdf.
3. T. D. Control and Complications Trial Research Group, "The effect of intensive treatment of diabetes on the development and progression of long-term complications in insulin-dependent diabetes mellitus," *N. Engl. J. Med.* **329**, 977-986 (1993).
4. T. Wysocki, "Impact of blood glucose monitoring on diabetic control: obstacles and interventions," *J. Behav. Med.* **12**, 183-205 (1989).
5. T. Koschinsky and L. Heinemann, "Sensors for glucose monitoring: technical and clinical aspects," *Diabetes Metab. Res. Rev.* **17**, 113-123 (2001).
6. S. A. Weinzimer and W. V. Tamborlane, "Sensor-augmented pump therapy in type 1 diabetes," *Curr. Opin. Endocrinol. Diabetes Obes.* **15**, 118-122 (2008).
7. M. Rigla, M. E. Hernando, E. J. Gomez, E. Bruges, G. Garcia-Saez, I. Capel, B. Pons, and A. de Leiva, "Real-time continuous glucose monitoring together with telemedical assistance improves glycemic control and glucose stability in pump-treated patients," *Diabetes Technol. Ther.* **10**, 194-199 (2008).

8. JDRF CGM Study Group, "JDRF randomized clinical trial to assess the efficacy of real-time continuous glucose monitoring in the management of type 1 diabetes: Research Design and Methods," *Diabetes Technol. Ther.* **10**, 310-321 (2008).
9. G. McGarraugh, "The chemistry of commercial continuous glucose monitors," *Diabetes Technol. Ther.* **11**, S-17 - S-24 (2009).
10. T. Henning, "Commercially available continuous glucose monitoring systems," in *In Vivo Glucose Sensing*, D. Cunningham and J. Stenken eds. (Wiley, 2002), pp. 113-156.
11. S. A. Weinzimer, "PENDRA: the once and future noninvasive continuous glucose monitoring device," *Diabetes Technol. Ther.* **6**, 442-444 (2004).
12. A. Pfützner, A. Caduff, M. Larbig, T. Schrepfer, and T. Forst, "Impact of posture and fixation technique on impedance spectroscopy used for continuous and noninvasive glucose monitoring," *Diabetes Technol. Ther.* **6**, 435-441 (2004).
13. I. M. E. Wentholt, J. B. L. Hoekstra, A. Zwart, and J. H. DeVries, "Pendra goes Dutch: lessons for the CE mark in Europe," *Diabetologia* **48**, 1055-1058 (2005).
14. Medtronic Minimed Inc., "The Guardian REAL-Time Continuous Glucose Monitoring System," <http://www.minimed.com/products/insulinpumps/faq/#a6>.
15. R. L. Weinstein, S. L. Schwartz, R. L. Brazg, J. R. Bugler, T. A. Peyser and G. V. McGarraugh, "Accuracy of the 5-day FreeStyle Navigator continuous glucose monitoring system: comparison with frequent laboratory reference measurements," *Diabetes Care* **30**, 1125-1130 (2007).

16. I. Gabriely, R. Wozniak, M. Mevorach, J. Kaplan, Y. Aharon, and H. Shamoon, "Transcutaneous glucose measurement using near-infrared spectroscopy during hypoglycemia," *Diabetes Care* **22**, 2026-2032 (1999).
17. K. H. Hazen, M. A. Arnold and G. W. Small, "Measurement of glucose in water with first-overtone near-infrared spectra," *Appl. Spectrosc.* **52**, 1597-1605 (1998).
18. K. H. Hazen, M. A. Arnold, and G. W. Small, "Measurement of glucose and other analytes in undiluted human serum with near-infrared transmission spectroscopy," *Anal. Chim. Acta* **371**, 255-267 (1998).
19. O. S. Khalil, S.-J. Yeh, M. G. Lowery, X. Wu, C. F. Hanna, S. Kantor, T.-W. Jeng, J. S. Kanger, R. A. Bolt, and F. F. de Mul, "Temperature modulation of the visible and near infrared absorption and scattering coefficients of human skin," *J. Biomed. Opt.* **8**, 191-205 (2003).
20. B. D. Cameron and G. L. Coté, "Noninvasive glucose sensing utilizing a digital closed-loop polarimetric approach," *IEEE Trans. Biomed. Eng.* **44**, 1221-1227 (1997).
21. B. D. Cameron, H. W. Gorde, B. Satheesan, and G. L. Coté, "The use of polarized laser light through the eye for noninvasive glucose monitoring," *Diabetes Technol. Ther.* **1**, 135-143 (1999).
22. J. S. Baba, B. D. Cameron, S. Theru, and G. L. Coté, "Effect of temperature, pH, and corneal birefringence on polarimetric glucose monitoring in the eye," *J. Biomed. Opt.* **7**, 321-328 (2002).

23. B. D. Cameron and H. Anumula, "Development of a real-time corneal birefringence compensated glucose sensing polarimeter," *Diabetes Technol. Ther.* **8**, 156-164 (2006).
24. Q. Wan, G. L. Coté, and J. B. Dixon, "Dual-wavelength polarimetry for monitoring glucose in the presence of varying birefringence," *J. Biomed. Opt.* **10**, 024029 (2005).
25. B. H. Malik and G. L. Coté, "Real-time, closed-loop dual-wavelength optical polarimetry for glucose monitoring," *J. Biomed. Opt.* **15**, 017002 (2010).
26. A. M. Enejder, T.-W. Koo, J. Oh, M. Hunter, S. Sasic, M. S. Feld, and G. L. Horowitz, "Blood analysis by Raman spectroscopy," *Opt. Lett.* **27**, 2004-2006 (2002).
27. A. M. Enejder, T. G. Seccina, J. Oh, M. Hunter, W. C. Shih, S. Sasic, G. L. Horowitz, and M. S. Feld, "Raman spectroscopy for noninvasive glucose measurements," *J. Biomed. Opt.* **10**, 031114 (2005).
28. M. Ren and M. Arnold, "Comparison of multivariate calibration models for glucose, urea, and lactate from near-infrared and Raman spectra," *Anal. Bioanal. Chem.* **387**, 879-888 (2007).
29. O. Lyandres, J. M. Yuen, N. C. Shah, R. P. VanDuyne, J. T. Walsh, and M. R. Glucksberg, "Progress toward an in vivo surface-enhanced Raman spectroscopy glucose sensor," *Diabetes Technol. Ther.* **10**, 257-265 (2008).
30. B. H. Malik and G. L. Coté, "Real-time dual wavelength polarimetry for glucose sensing," *Proc. SPIE* **7186**, 718694 (2009).

31. G. Mazarevica, T. Freivalds, and A. Jurka, "Properties of erythrocyte light refraction in diabetic patients," *J. Biomed. Opt.* **7**, 244-247 (2002).
32. A. Tura, A. Maran, and G. Pacini, "Non-invasive glucose monitoring: assessment of technologies and devices according to quantitative criteria," *Diabetes Res. Clin. Pract.* **77**, 16-40 (2007).
33. R. M. Waynant and V. M. Chenault, "Overview of non-invasive fluid glucose measurement using optical techniques to maintain glucose control in diabetes mellitus," *IEEE LEOS Newsletter* **12**, 3-6 (1998).
34. P. H. N. Oomen, G. D. Kant, R. P. F. Dullaart, W. D. Reitsma, and A. J. Smit, "Acute hyperglycemia and hyperinsulinemia enhance vasodilatation in type 1 diabetes mellitus without increasing capillary permeability and inducing endothelial dysfunction," *Microvasc. Res.* **63**, 1-9 (2002).
35. V. M. Monnier, O. Bautista, D. Kenny, D. R. Sell, J. Fogarty, W. Dahms, P. A. Cleary, J. Lachin, and S. Genuth, "Skin collagen glycation, glycooxidation, and crosslinking are lower in subjects with long-term intensive versus conventional therapy of type 1 diabetes: relevance of glycated collagen products versus HbA1c as markers of diabetic complications," *Diabetes* **48**, 870-880 (1999).
36. K. E. Shafer-Peltier, C. L. Haynes, M. R. Glucksberg, and R. P. Van Duyne, "Toward a glucose biosensor based on surface-enhanced Raman scattering," *J. Am. Chem. Soc.* **125**, 588-593 (2002).
37. A. F. Bell, L. D. Barron, and L. Hecht, "Vibrational Raman optical activity study of d-glucose," *Carbohydr. Res.* **257**, 11-24 (1994).

38. J. Chaiken, W. F. Finney, X. Yang, P. E. Knudson, K. P. Peterson, C. M. Peterson, R. S. Weinstock, and D. Hagrman, "Progress in the noninvasive in-vivo tissue-modulated Raman spectroscopy of human blood," *Proc. SPIE* **4254**, 216 (2001).
39. I. Barman, C.-R. Kong, G. P. Singh, R. R. Dasari, and M. S. Feld, "Accurate spectroscopic calibration for noninvasive glucose monitoring by modeling the physiological glucose dynamics," *Anal. Chem.* **82**, 6104-6114 (2010).
40. N. C. Dingari, I. Barman, J. W. Kang, C.-R. Kong, R. R. Dasari, and M. S. Feld, "Wavelength selection-based nonlinear calibration for transcutaneous blood glucose sensing using Raman spectroscopy," *J. Biomed. Opt.* **16**, 087009 (2011).
41. P. J. Aarnoutse and J. A. Westerhuis, "Quantitative Raman reaction monitoring using the solvent as internal standard," *Anal. Chem.* **77**, 1228-1236 (2005).
42. H. Zeng, C. MacAulay, D. I. McLean, B. Palcic, and H. Lui, "The dynamics of laser-induced changes in human skin autofluorescence—experimental measurements and theoretical modeling," *Photochem. Photobiol.* **68**, 227-236 (1998).
43. M. S. Boyne, D. M. Silver, J. Kaplan, and C. D. Saudek, "Timing of changes in interstitial and venous blood glucose measured with a continuous subcutaneous glucose sensor," *Diabetes* **52**, 2790-2794 (2003).
44. E. Cengiz and W. V. Tamborlane, "A tale of two compartments: interstitial versus blood glucose monitoring," *Diabetes Technol. Ther.* **11**, S-11-S-16 (2009).

45. E. Kulcu, J. A. Tamada, G. Reach, R. O. Potts, and M. J. Lesho, "Physiological differences between interstitial glucose and blood glucose measured in human subjects," *Diabetes Care* **26**, 2405 (2003).
46. B. D. Cameron, J. S. Baba, and G. L. Coté, "Measurement of the glucose transport time delay between the blood and aqueous humor of the eye for the eventual development of a noninvasive glucose sensor," *Diabetes Technol. Ther.* **3**, 201-207 (2001).
47. S. Pohjola, "The glucose content of the aqueous humor in man," *Acta. Ophthalmol.* **88**, 11-80 (1966).
48. M. A. Melin, "On the manufacture of sugar in Belgium," *ARCHIVE: Proceedings of the Institution of Mechanical Engineers* **34**, 368-420 (1883).
49. B. Rabinovitch, W. F. March, and R. L. Adams, "Noninvasive glucose monitoring of the aqueous humor of the eye: Part I. Measurement of very small optical rotations," *Diabetes Care* **5**, 254-258 (1982).
50. W. F. March, B. Rabinovitch, and R. L. Adams, "Noninvasive glucose monitoring of the aqueous humor of the eye: II. Animal studies and the scleral lens," *Diabetes Care* **5**, 259-265 (1982).
51. G. L. Coté, M. D. Fox, and R. B. Northrop, "Noninvasive optical polarimetric glucose sensing using a true phase measurement technique," *IEEE Trans. Biomed. Eng.* **39**, 752-756 (1992).
52. M. J. Goetz, Jr., "Microdegree polarimetry for glucose detection," M.S. Thesis, University of Connecticut, Storrs, CT 06269 (1992).

53. T. W. King, G. L. Coté, R. McNichols, and M. J. Goetz Jr, "Multispectral polarimetric glucose detection using a single Pockels cell," *Opt. Eng.* **33**, 2746-2753 (1994).
54. C. Chou, C. Y. Han, W. C. Kuo, Y. C. Huang, C. M. Feng, and J. C. Shyu, "Noninvasive glucose monitoring in vivo with an optical heterodyne polarimeter," *Appl. Opt.* **37**, 3553-3557 (1998).
55. G. L. Coté, H. Gorde, J. Janda, and B. D. Cameron, "Multispectral polarimetric system for glucose monitoring," *Proc. SPIE* **3253**, 36-40 (1998).
56. R. R. Ansari, S. Bockle, and L. Rovati, "New optical scheme for a polarimetric-based glucose sensor," *J. Biomed. Opt.* **9**, 103-115 (2004).
57. R. Rawer, W. Stork, and K. D. Muller-Glaser, "Polarimetric methods for measurement of intra ocular glucose concentration," *Biomed. Tech. (Berl)* **47**, Suppl 1 Pt 1, 186-188 (2002).
58. R. Rawer, W. Stork, and C. F. Kreiner, "Non-invasive polarimetric measurement of glucose concentration in the anterior chamber of the eye," *Graefes Arch. Clin. Exp. Ophthalmol.* **242**, 1017-1023 (2004).
59. L. Pasteur, *Researches on the molecular asymmetry of natural organic products microform* (The Alembic Club, 1905).
60. F. Ciardelli and P. Salvadori, eds., *Fundamental Aspects and Recent Developments in Optical Rotatory Dispersion and Circular Dichroism* (Heyden and Son Ltd, 1973).
61. A. C. Guyton, *Textbook of medical physiology* (Saunders, 1991).

62. E. Hecht, *Optics* (Addison Wesley, 2001).
63. J. Krachmer, M. Mannis, and E. Holland, *Cornea* (Elsevier Mosby, 2011).
64. D. J. Donohue, B. J. Stoyanov, R. L. McCally, and R. A. Farrell, "Numerical modeling of the cornea's lamellar structure and birefringence properties," *J. Opt. Soc. Am. A* **12**, 1425-1438 (1995).
65. M. Born and E. Wolf, *Principles of Optics* (Cambridge University Press, 1998).
66. P. Kaufman and A. Alm, eds., *Adler's Physiology of the Eye* (Mosby, 2003).
67. D. M. Maurice, "The structure and transparency of the cornea," *J. Physiol.* **136**, 263-286 (1957).
68. H. F. Edelhauser, "The balance between corneal transparency and edema: the Proctor Lecture," *Invest. Ophthalmol. Vis. Sci.* **47**, 1755-1767 (2006).
69. J. L. Cox, R. A. Farrell, R. W. Hart, and M. E. Langham, "The transparency of the mammalian cornea," *J. Physiol.* **210**, 601-616 (1970).
70. R. A. Farrell, R. L. McCally, and P. E. R. Tatham, "Wave-length dependencies of light scattering in normal and cold swollen rabbit corneas and their structural implications," *J. Physiol.* **233**, 589-612 (1973).
71. R. N. Weinreb, C. Bowd, D. S. Greenfield, and L. M. Zangwill, "Measurement of the magnitude and axis of corneal polarization with scanning laser polarimetry," *Arch. Ophthalmol.* **120**, 901-906 (2002).
72. C. K. Hitzengerger, E. Gotzinger, and M. Pircher, "Birefringence properties of the human cornea measured with polarization sensitive optical coherence tomography," *Bull. Soc. belge Ophtalmol.* **302**, 153-168 (2006).

73. R. N. Weinreb, F. A. Medeiros, L. M. Zangwill, and C. Bowd, "Comparison of the GDx VCC scanning laser polarimeter, HRT II confocal scanning laser ophthalmoscope, and stratus OCT optical coherence tomograph for the detection of glaucoma," *Arch. Ophthalmol.* **122**, 827-837 (2004).
74. A. Stanworth and E. J. Naylor, "The polarization optics of the isolated cornea," *Br. J. Ophthal.* **34**, 201-211 (1950).
75. A. Stanworth and E. J. Naylor, "Polarized light studies of the cornea," *J. Exp Biol.* **30**, 160-163 (1953).
76. G. J. Van Blokland and S. C. Verhelst, "Corneal polarization in the living human eye explained with a biaxial model," *J. Opt. Soc. Am. A* **4**, 82-90 (1987).
77. R. W. Knighton and X. R. Huang, "Linear birefringence of the central human cornea," *Invest. Ophthalmol. Vis. Sci.* **43**, 82-86 (2002).
78. R. W. Knighton, X.-R. Huang, and L. A. Cavuoto, "Corneal birefringence mapped by scanning laserpolarimetry," *Opt. Express* **16**, 13738-13751 (2008).
79. L. J. Bour and N. J. Lopes Cardozo, "On the birefringence of the living human eye," *Vision Res.* **21**, 1413-1421 (1981).
80. J. M. Bueno and F. Vargas-Martín, "Measurements of the corneal birefringence with a liquid-crystal imaging polariscope," *Appl. Opt.* **41**, 116-124 (2002).
81. J. W. Jaronski and H. T. Kasprzak, "Linear birefringence measurements of the in vitro human cornea," *Ophthalmic Physiol. Opt.* **23**, 361-369 (2003).

82. G. P. Misson, "Circular polarization biomicroscopy: a method for determining human corneal stromal lamellar organization in vivo," *Ophthalmic Physiol. Opt.* **27**, 256-264 (2007).
83. J. W. Jaronski and H. T. Kasprzak, "Generalized Algorithm for Photoelastic Measurements Based on Phase-Stepping Imaging Polarimetry," *Appl. Opt.* **38**, 7018-7025 (1999).
84. K. B. Doyle, J. M. Hoffman, V. L. Genberg, and G. J. Michels, "Stress birefringence modeling for lens design and photonics," in *International Optical Design Conference, 2002 OSA Technical Digest Series* (Optical Society of America, 2002), paper IWC1.
85. D. Atchison and G. Smith, *Optics of the Human Eye* (Butterworth Heinemann, 2000).
86. H.-L. Liou and N. A. Brennan, "Anatomically accurate, finite model eye for optical modeling," *J. Opt. Soc. Am. A* **14**, 1684-1695 (1997).
87. R. C. Weast, ed., *Handbook of Chemistry and Physics* (CRC Press, 1974).
88. T. J. Y. Wang and F. A. Bettelheim, "Comparative birefringence of cornea," *Comp. Biochem. Physiol. A Physiol.* **51**, 89-94 (1975).
89. P. A. Williams, "Rotating-wave-plate Stokes polarimeter for differential group delay measurements of polarization-mode dispersion," *Appl. Opt.* **38**, 6508-6515 (1999).
90. J.-M. Liu, *Photonic devices* (Cambridge, 2005).

91. Q. Wan, G. L. Coté, and J. B. Dixon, "Dual-wavelength polarimetry for monitoring glucose in the presence of varying birefringence," *J. Biomed. Opt.* **10**, 024029 (2005).
92. G. F. Franklin, D. J. Powell, and A. Emami-Naeini, *Feedback Control of Dynamic Systems* (Prentice Hall, 2001).
93. B. H. Malik and G. L. Coté, "Modeling the corneal birefringence of the eye toward the development of a polarimetric glucose sensor," *J. Biomed. Opt.* **15**, 037012 (2010).
94. J. Arnbjerg and T. Eriksen, "Increased glucose content in the aqueous humour caused by the use of xylazine," *Ophthalmic Res.* **22**, 265-268 (1990).
95. K. Chalabi, M. Schutte, and M. Reim, "Alterations of glucose levels in the blood and the anterior eye segment of rabbits exposed to ketamine-xylazine anaesthesia," *Ophthalmic Res.* **19**, 289-291 (1987).
96. S. Hodson, C. Wigham, L. Williams, K. R. Mayes, and M. V. Graham, "Observations on the human cornea in vitro," *Exp. Eye Res.* **32**, 353-360 (1981).
97. B. L. Boyce, J. M. Grazier, R. E. Jones, and T. D. Nguyen, "Full-field deformation of bovine cornea under constrained inflation conditions," *Biomaterials* **29**, 3896-3904 (2008).
98. N. S. Lipman, R. P. Marini, and S. E. Erdman, "A comparison of ketamine/xylazine and ketamine/xylazine/acepromazine anaesthesia in the rabbit," *Lab. Anim. Sci.* **40**, 395-398 (1990).

APPENDIX A

CODE V PROGRAM FILE

Surface #	Surface Name	Surface Type	Y Radius	Thickness	Glass	Refract Mode
Object		Sphere	Infinity	Infinity		Refract
Stop		Sphere	Infinity	0.0000	AIR	Refract
2		Sphere	Infinity	10.0000	WATER_SPE	Refract
3	Cornea IN	Sphere	7.7000	0.9000	376000.55	Refract
4	Aq. Humor	Sphere	6.8000	13.6000	WATER_SPE	Refract
5	Aq. Humor	Sphere	-6.8000	0.9000	376000.55	Refract
6	Cornea OU	Sphere	-7.7000	5.0000	WATER_SPE	Refract
7		Sphere	Infinity	5.0000	WATER_SPE	Refract
8		Sphere	Infinity	0.5000	WATER_SPE	Refract
Image		Sphere	Infinity	0.0000	WATER_SPE	Refract

End Of Data

VITA

Name: Bilal Hameed Malik

Address: Department of Biomedical Engineering,
5045 Emerging Technologies Building
3120 TAMU,
College Station, TX 77843-3120

Email Address: malik@tamu.edu

Education: B.S. Engineering Sciences, GIK Institute, Pakistan, 2002

M.S. Electrical Engineering, Texas A&M University, 2006